Precambrian Research 336 (2020) 105492

Contents lists available at ScienceDirect

Precambrian Research

journal homepage: www.elsevier.com/locate/precamres

Petrology and geochemistry of TTG and K-rich Paleoproterozoic Birimian granitoids of the West African Craton (Ghana): Petrogenesis and tectonic implications

Patrick Asamoah Sakyi[a,*], Rauda Adam Addae[a,b], Ben-Xun Su[c], Samuel Boakye Dampare[d], Emmanuel Abitty[e], Ben-Can Su[f], Bin Liu[f], Daniel Kwadwo Asiedu[a]

[a] Department of Earth Science, School of Physical and Mathematical Sciences, University of Ghana, Legon-Accra, Ghana
[b] Ghana Geological Survey Authority, P.O. Box M80, Accra, Ghana
[c] Key Laboratory of Mineral Resources, Institute of Geology and Geophysics, Chinese Academy of Sciences, P.O. Box 9825, Beijing 100029, China
[d] School of Nuclear and Allied Sciences, University of Ghana, Kwabenya-Accra, Ghana
[e] Dipartimento di Fisica é Geologia, Universita degli studi di Perugia, 1-06123 Perugia, Italy
[f] Changqing Oil Field Company, Oil Production Plant No. 8, Xi'an 710018, China

ARTICLE INFO

Keywords:
Paleoproterozoic
Birimian
TTGs
K-rich granitoids
West African Craton
Bole-Nangodi Belt

ABSTRACT

We conducted petrologic, geochemical and isotopic studies on Paleoproterozoic Birimian granitoids that intrude the Bole-Nangodi Belt in northern Ghana, in southeastern West African Craton (WAC), to constrain the geodynamic evolution of the Birimian Supergroup. The rocks are potassic (K)-rich granitoids (KRGs), tonalities, trondhjemites, granodiorites (TTGs), pegmatite and aplite. The K_2O contents of the KRGs are up to 5 wt%, with generally high concentrations of Rb, Ba, Sr, Cr and Ni. They are highly fractionated calc-alkaline I-type granitoids, enriched in LILE and LREE relative to HREE and HFSE. Chondrite-normalized REE diagrams indicate fractionated LREE (average La_N/Sm_N = 5.05) and HREE (Gd_N/Yb_N = 4.56) patterns, with slight negative Eu anomalies (average Eu/Eu* = 0.75). This may indicate an evolved magma source with varying degrees of plagioclase fractionation. The KRGs share similar geochemical characteristics with the TTGs into which they intrude. Both rock types are characterized by Ba and Th enrichment and depletion in Nb-Ta, Zr-Hf, and Ti, which are typical characteristics of subduction-related magmas. The pegmatite-aplite association is slightly geochemically different and may have formed at a time later than the KRGs. The ε_{Nd}(2.1 Ga) values range from + 0.90 to + 1.24 and −0.86 to + 1.37 respectively for the TTGs and KRGs, with T_{DM1} ages of 2.34–2.38 Ga and 2.36–2.53 Ga and T_{DM2} ages of 2.21–2.24 Ga and 2.22–2.39 Ga respectively. These indicate their juvenile character, possibly a depleted mantle source with minor contributions from a pre-Birimian (or Archean?) crustal material in their source material(s). The TTGs and KRGs are volcanic arc granites (VAG) and *syn*-collisional (Syn-COLG) granites, with formation temperatures and pressures of ~640–750 °C and ~2–6 kbar respectively. Based on the high temperatures, I-type signature, calc-alkaline nature and other geochemical characteristics, we infer that the TTGs, KRGs and pegmatite-aplite association developed under high oxygen fugacity conditions in an orogenic tectonic setting related to subduction. Thus, our geochemical and isotopic results are consistent with an island arc tectonic setting arising from subduction–accretion processes, which are typical for the Paleoproterozoic terranes of the WAC. These processes may have contributed to the amalgamation of the Columbia (Nuna) supercontinent during the Paleoproterozoic (2.1–1.8 Ga) orogeny.

1. Introduction

The West African Craton (WAC) contains numerous granitoid plutons of various generations. The Bole-Nangodi greenstone Belt, which forms part of the southeastern portion of the Paleoproterozoic block of the Man Shield of the WAC hosts various types of granitoid rocks, all of which have been affected by the Eburnean Orogeny (ca. 2.1–2.0 Ga) (e.g. Liégeois et al., 1991). The Bole-Nangodi Belt consists of potassic granitoids that are dominantly granites, TTGs, pegmatite and aplite. Granitoid plutons form essential constituents of the continental crust and orogenic zones, and they are highly compositionally diverse (Altherr et al., 2000; Eleftherriadis and Koroneos, 2003; Christofides

* Corresponding author.
E-mail address: pasakyi@ug.edu.gh (P.A. Sakyi).

https://doi.org/10.1016/j.precamres.2019.105492
Received 12 October 2018; Received in revised form 24 September 2019; Accepted 11 October 2019
Available online 14 October 2019
0301-9268/

et al., 2007). Granitoids of the Bole-Nangodi and Wa-Lawra Belts (northern Ghana) are only recently being studied (Sakyi et al., 2014; Block et al., 2016a, 2016b; Abitty et al., 2016). Sakyi et al. (2014) reported that the granitoids of the Wa-Lawra Belt are I-type and may have been derived from an evolved magma in a subduction-related tectonic setting. Magmatism over a time span of ca. 81 Ma (ca. 2213–2130 Ma) indicates that the melts responsible for the formation of the granitoids of the Wa-Lawra Belt were probably derived from the same source and were affected by the same mantle and crustal processes that occurred at an earlier stage of the Eburnean Orogeny (Sakyi et al., 2014).

According to Block et al. (2016b) all the different rock types that make up the Paleoproterozoic crust of northern Ghana were formed together over a prolonged period of ca. 100 Ma, between ca. 2.21 and 2.11 Ga, where the TTGs were derived from the reworking of low-K hydrous mafic crust. The more felsic rock types were formed by reworking of older felsic crustal rocks. A study of the KRGs of the Bole-Nangodi Belt by Abitty et al. (2016) revealed that they are I-type granitoids that were generated under hydrous conditions of melting with magma mixing, assimilation and fractional crystallization playing a key role, and subsequently emplaced in a volcanic arc geotectonic environment. Abitty et al. (2016) inferred that even though the KRGs are I-type granitoids, they show some geochemical signatures, similar to A-type granitoids, suggesting an arc-back-arc tectonic setting for the KRGs of the Bole-Nangodi Belt. However, the integration of field work, petrography and whole-rock major and trace element geochemistry of a limited sample size (Abitty et al., 2016) may not be enough to provide adequate insights into the geodynamic environment of emplacement and petrogenetic implications of the KRGs of the Bole-Nangodi Belt of Ghana.

The peculiar K-rich nature of the granitoids in the Bole-Nangodi Belt and the relationship between their geochemistry and source material composition are key to understanding the geodynamic evolution of the Paleoproterozoic terrane of the WAC (Huang et al., 2010). According to Huang et al. (2010) the geochemical characteristics of K-rich rocks may provide a genetic link between continental collision and continued post-collisional processes. This makes it possible to understand the origin and evolution of the continental crust (Eleftherriadis and Koroneos, 2003; Eglinger et al., 2017; Wane et al., 2018). Most of the Paleoproterozoic Birimian rocks in the Bole-Nangodi Belt do not show any significant variation in geochemical characteristics. Thus, they may be products of a similar source with varying degrees of evolution and generated in similar tectonic settings (e.g. Sakyi et al., 2014; Block et al., 2016b). In order to adequately understand the geodynamic evolution and provide new perspectives on the petrogenesis and tectonic implications of the KRGs and its associated rocks, we present detailed petrographic studies and in situ major element analysis of selected minerals as well as new whole-rock geochemical and isotopic data of the KRGs and associated rocks of the Bole-Nangodi Belt.

2. Geological setting

The WAC is composed of two Precambrian shields, namely; the Reguibat shield to the north and the Leo-Man Shield to the south. Both shields are subdivided into a western domain (Kenema-Man of Archaean age) (Fig. 1), characterized by Liberian (ca. ~2.75 Ga), Leonean (ca. ~2.95 Ga) and pre-Leonean (ca. ~3.1 Ga) orogenic events (Wright et al., 1985), and a central-eastern domain (Baoulé-Mossi/Birimian of Paleoproterozoic age), characterized by the Eburnean (ca. ~2.2–2.0 Ga) orogeny (e.g. Feybesse et al., 2006; Vidal et al., 2009; Hein, 2010; de De Kock et al., 2011).

Ghana occupies the southeastern portion of the WAC. About one-third of the entire geology of Ghana is underlain by Paleoproterozoic Birimian rocks, consisting of six greenstone Belts, namely; Kibi-Winneba, Ashanti, Sefwi, Bui, Bole-Nangodi (all of which trend NE-SW) and the N-S trending Lawra Belt (Fig. 2). The other two-thirds is occupied mainly by the Voltaian sedimentary rocks and Dahomeyide rock units. The greenstone Belts consist basically of metavolcanic rocks and are separated by sedimentary basins made up of metasedimentary rocks. Granitoids that intrude the volcanic Belts are metaluminous and Na-rich, whereas the sedimentary basins are intruded by peraluminous, calc-alkaline and ferroan granitoids (e.g. Leube et al., 1990; Hirdes et al., 1992; Taylor et al., 1992). The Belt and basin granitoids are mainly the Dixcove-type hornblende granitoid and Cape Coast-type biotite granitoid respectively. Also occurring locally are the Winneba and the Bongo/Banso granitoids (e.g. Leube et al., 1990; Nyarko et al., 2012; Petersson et al., 2016). This study focuses on the Bongo granitoids, mainly because they have received very little attention, and therefore, have provided only little contribution to the petrogenesis and tectonic implication of the Birimian rocks of Ghana. U-Pb zircon dating of some belt-type granitoids yielded ages of ca. 2179 ± 2 Ma and ca. 2172 ± 2 Ma (Hirdes et al., 1992). Recently dated granitoid rocks from the Lawra volcanic Belt of northwestern Ghana yielded U-Pb zircon ages of ca. 2213–2130 Ma (Sakyi et al., 2014), whilst Anum et al. (2015) also obtained ages of ca. 2191–2127 Ma for granitoids in the Kibi-Winneba Belt of southern Ghana.

The Birimian geology of northern Ghana can be divided into three crustal blocks. They include the western block (Wa-Lawra Belt), the northern block (Koudougou-Tumu granitoid domain, the Julie Belt and the Bole-Bulenga domain), and the southern and eastern blocks (the Maluwe domain, Abulembire domain, Bawku granitoid domain and the Nangodi Belt) (Block et al., 2016b). The Bole-Nangodi Belt (Inset in Fig. 2) is characterized by volcanic lobes, made up of basaltic flow, andesitic lavas, pyroclastics and sedimentary rocks and intruded in parts by granitoids. Rocks flanking the Bole-Nangodi Belt include tonalite and granodiorite gneisses, dioritic and granodioritic gneisses, paragneisses, and foliated hornblende granodiorite (Attoh, 1982). Also present in the Bole-Nangodi Belt is a succession of shales, greywacke and gondites alternating with MORB-type basalts, and overlain by calc-alkaline andesitic to rhyolitic lava flows (e.g. Block et al., 2016b).

3. Analytical methods

All analyses were carried out at the Institute of Geology and Geophysics, Chinese Academy of Sciences, Beijing, China. Sample information, locations, rock types and basic field description can be found in Table S1. The rock samples were cut into smaller slabs, polished, mounted on a glass slide using Canada Balsam, trimmed and ground until a thickness of 0.03 mm was obtained. Forty-five samples were analyzed for their whole-rock major and trace element compositions. The major element compositions were obtained using Shimadzu XRF-1500 instrument on fused glass disks. Approximately 0.5 g of rock powder was mixed with 5 g of $Li_2B_4O_7$, and 3 drops of NH_4Br and the mixture was fused in a furnace to form a glass disk. The disks were then analyzed for major element contents at a current and voltage of 50 mA and 50 kV, respectively. For the trace element analysis, about 100 mg of crushed whole-rock powder was dissolved in 2 ml HF and 1 ml HNO_3 in a closed Teflon bomb, which was heated on a hot plate at ~ 140 °C, then opened and subsequently evaporated to dryness to remove silica. Thereafter, 1.5 ml HF, 1.5 ml HNO_3 and 10 ml $HClO_4$ were added to the Teflon bomb. The bomb was placed in a steel jacket and heated in an oven at 190 °C for 5 days to completely dissolve the sample. This was followed by dry down and addition of concentrated HNO_3 to form nitrates, followed by a final evaporation. Thereafter, 2 ml 50% HNO_3 was added to the Teflon bomb, which was subsequently put into the jacket again and heated to 150 °C for 24 h. Finally, 0.5 g Rh (1 ppm) was added to the solution as an internal standard, and the solution was diluted by a factor of 500. The solutions were then analyzed by ICP-MS using an Agilent 7000a system. Precisions of the ICP-MS analyses were generally better than 5%. Analytical uncertainties were 1–3% relative to elements present in concentrations greater than 1 wt%, and about 10% relative to elements present in concentrations less than 1 wt%. Elements detection limits are reported in Jin and Zhu (2000) and

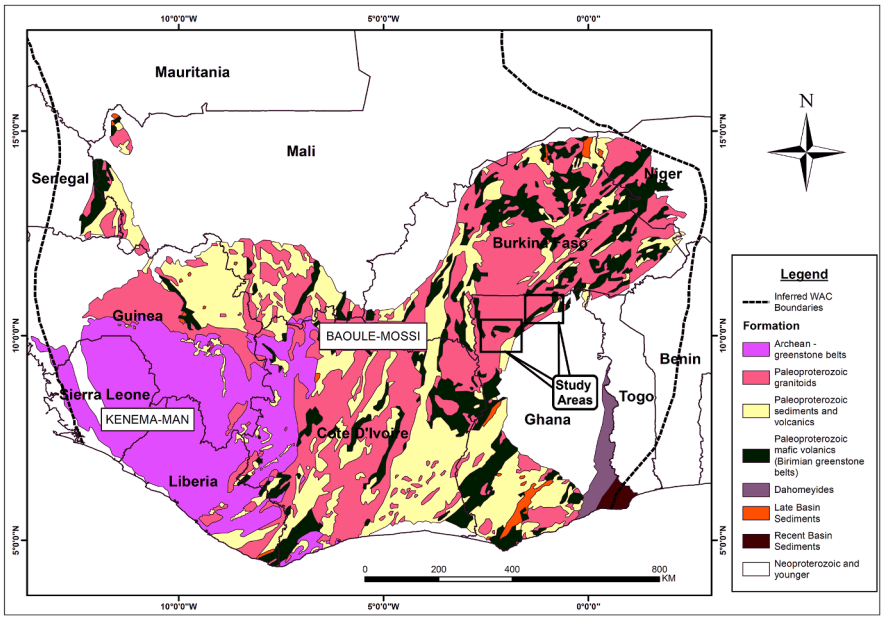

Fig. 1. Simplified geological map of the Leo-Man Shield of the West African Craton, showing areas underlain by Paleoproterozoic Birimian crust (Milési et al., 1992).

reproduced in Table S2. Detail description of analytical procedures is reported in Chu et al. (2009).

Rb-Sr and Sm-Nd isotopic analyses were performed on ten samples, using a VG-354 Thermal Ionization Magnetic Sector Mass Spectrometer. The chemical separation and isotopic measurement procedures followed that of Zhang et al. (2002). Mass fractionation corrections for Sr and Nd isotopic ratios were based on values of $^{86}Sr/^{88}Sr = 0.1194$ and $^{146}Nd/^{144}Nd = 0.7219$ (Chu et al., 2011). Uncertainties in Rb/Sr and Sm/Nd ratios were less than 2% and 0.5%, respectively.

Nineteen rock samples were selected for mineral chemistry analyses by the wavelength-dispersive spectrometry method, using JEOL JXA8100 electron probe microanalyzer (EPMA) operating at an accelerating voltage of 15 kV and 10 nA beam current, 5 μm beam spot and 10–30 s counting time on peak. Natural mineral samples namely; jadeite ($NaAlSiO_6$) for Na, Al and Si, rhodonite ($MnSiO_3$) for Mn, sanidine ($KAlSi_3O_8$) for K, garnet ($Fe_3Al_2Si_3O_{12}$) for Fe, Cr-diopside (Mg, Cr) $CaSi_2O_6$ for Ca, and olivine (Mg, Fe)$_2SiO_4$ for Mg, as well as synthetic minerals namely rutile for Ti, 99.7% Cr_2O_3 for Cr, and Ni_2Si for Ni, were used for standard calibration (Su et al., 2014), and a program based on the ZAF procedure was used for matrix corrections. The precisions of all analyzed elements were better than 1–2%.

4. Results

4.1. Petrography

The studied rocks can be separated into three distinct groups as follows; K-rich granitoids (KRGs), tonalities-trondhjemites-granodiorites (TTGs), and pegmatite-aplite rock association.

4.1.1. K-rich Granitoid (KRG)

The KRGs consist mainly of granites with some granodiorites and adamellites. The granites (Fig. 3a) include granite (s.s.), two-mica granite, pyroxene granite, hornblende granite, *meta*-granite and granitic gneiss (Table 1). The mineral grains of the granites are holocrystalline and granular with some slightly deformed types. The plagioclase and K-feldspar grains are prismatic, myrmekitic, perthitic, and incipiently recrystallized, with poorly preserved twin lamellae (Fig. 3b). The plagioclase and K-feldspar grains are zoned with sericitized zone planes, with the occurrence of cracked types mostly infilled by quartz and/or muscovite grains. The pyroxene grains are emerald to dark green in colour, and mainly euhedral to subhedral with few anhedral types. The hornblende grains are mostly brown with few green types that have poorly preserved cleavage planes (Fig. 3c), with some zoned types observed (Fig. 3d). Some of the hornblende grains are partially dissolved with their cavities infilled by apatite grains. Others are densely stuffed with titanite grains. Pleochroic haloes in biotite grains sometimes host titanite and zircon grains. Muscovite grains define the foliation in the *meta*-granite and granitic gneisses (Fig. 3e) and they are aligned with twin lamellae of some feldspar grains in these rocks. Biotite and muscovite grains are mostly interstitial, whereas the quartz grains are recrystallized and show preferred orientation in the meta-granite and granitic gneisses. Generally, the quartz grains are either cryptocrystalline, polycrystalline, interlocking, sutured or poikilitic, and show undulose extinction or are granulated at their boundaries. Some of granites are sheared, displaying bent mineral grains (e.g. biotite and plagioclase twin lamellae), and brecciated and fractured (microfaults) plagioclase grains (Fig. 3f). Also present in some granites are shredded and milled grains of biotite and muscovite, with common grain elongation, grain rotation and cracks. Accessory minerals include opaque oxide/sulphide, epidote, apatite, titanite, carbonate, zircon and fluorite.

The granodiorites (Fig. 4a) are composed of plagioclase, K-feldspar, muscovite and quartz (Tables 1 and 2). Accessories include opaque oxide/sulphide, titanite, zircon, epidote, carbonate and apatite. The grains are holocrystalline, coarse to serrated and granular. Pleochroic haloes of biotite occasionally host zoned grains of zircon. Muscovite inclusions in K-feldspar grains are usually aligned along twin lamellae. Quartz grains are in some cases interstitial, sutured and form vein-like structures (Fig. 4b). The grains are conchoidally fractured or cracked (so are epidote and titanite) with common grain boundary granulations (Fig. 4c). Some of the granodiorites are sheared with the occurrence of haphazardly oriented muscovite grains in the centrally altered cores of plagioclase and also around fresh plagioclase and K-feldspar grains (Fig. 4d). Bent and/or fractured plagioclase grains are common with biotite defining the plane of displacement. The hornblende grains are mostly zoned. The adamellite is composed of plagioclase, biotite, K-feldspar, muscovite and quartz (Tables 1 and 2). Accessories include opaque oxide/sulphide, titanite, epidote, hornblende and apatite, which are holocrystalline and granular. The quartz grains are

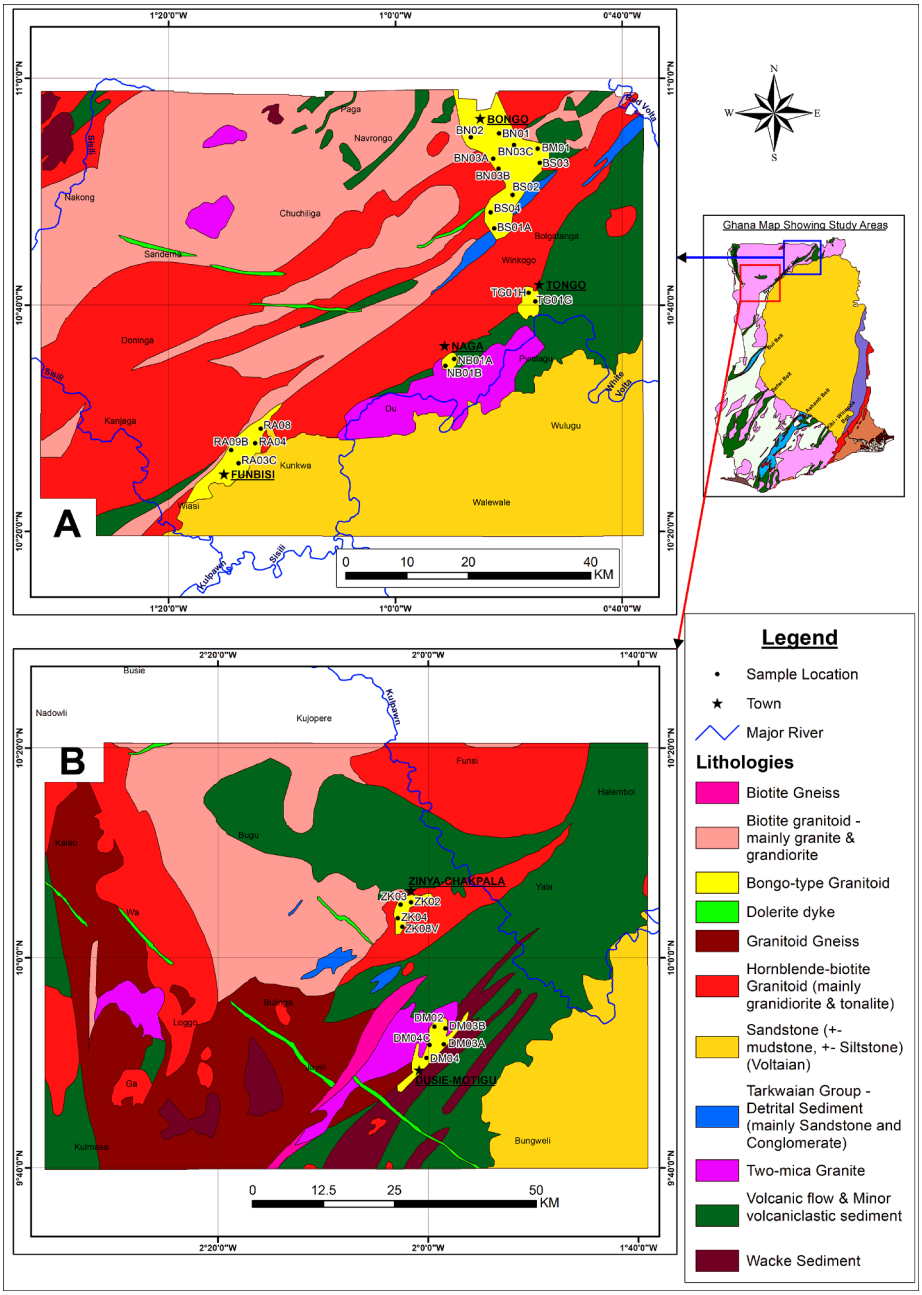

Fig. 2. Geological map of the Bole-Nangodi Belt showing the different rock types. Black dots represent sampling locations (after Abitty et al., 2016).

sometimes bent with incipient dissolution defining an axial plane.

4.1.2. Tonalite-Trondhjemite-Granodiorite (TTG)

The TTGs (Tables 1 and 2) are similar to the KRGs, except that the anorthite and albite plagioclase types have been partly or wholly sericitized. The presence of granulated and recrystallized quartz grains of the TTGs is indicative of shearing. K-feldspar, muscovite and biotite also occur in these rocks (Fig. 5b–d). Geochemically they are more sodic than the KRGs.

4.1.3. Pegmatite and aplite (P/A)

The pegmatite and aplite are composed of microcline, plagioclase, muscovite and quartz (Table 1). The grains are holocrystalline, coarse (pegmatite) and fine (aplite), and granular. The microcline grains are mostly altered to sericite, whereas the muscovite grains are mostly interstitial, displaying preferred orientation. The muscovite grains are clustered and bent in the aplite. Interstitial microcline grains are observed in the aplite. The quartz grains are sutured, polycrystalline, interstitial, brecciated and form weakly preserved veins (Fig. 6b and 6c). In the aplite, their boundaries display evidence of dissolution (Fig. 6d).

Results from mineral chemistry analyses (Table 3) indicate that the TTGs and KrGs are made up of various proportions of plagioclase such as anorthite (An_{90} to An_{100}), bytownite (An_{80} to An_{88}), andesine (~An_{44}) and albite (An_{0}) (Fig. 7a). Others are pyroxene (enstatite; $Wo_{0.1\text{-}0.3}$ $Fs_{30.0\text{-}41.9}$ $En_{57.9\text{-}69.6}$; KRGs only; Fig. 7b), hornblende (magnesio-hornblende; KRGs only; Fig. 7c), biotite (transition from Mg to Fe-rich types; Fig. 7f) and K-feldspar (orthoclase - ~Or_{98}; Fig. 7a) (Tables 2 and 3). The hornblende grains are calcic and magmatic (Fig. 7c and 7d).

4.2. Major and trace element geochemistry

4.2.1. KRG

The results of whole-rock major and trace element analyses of the

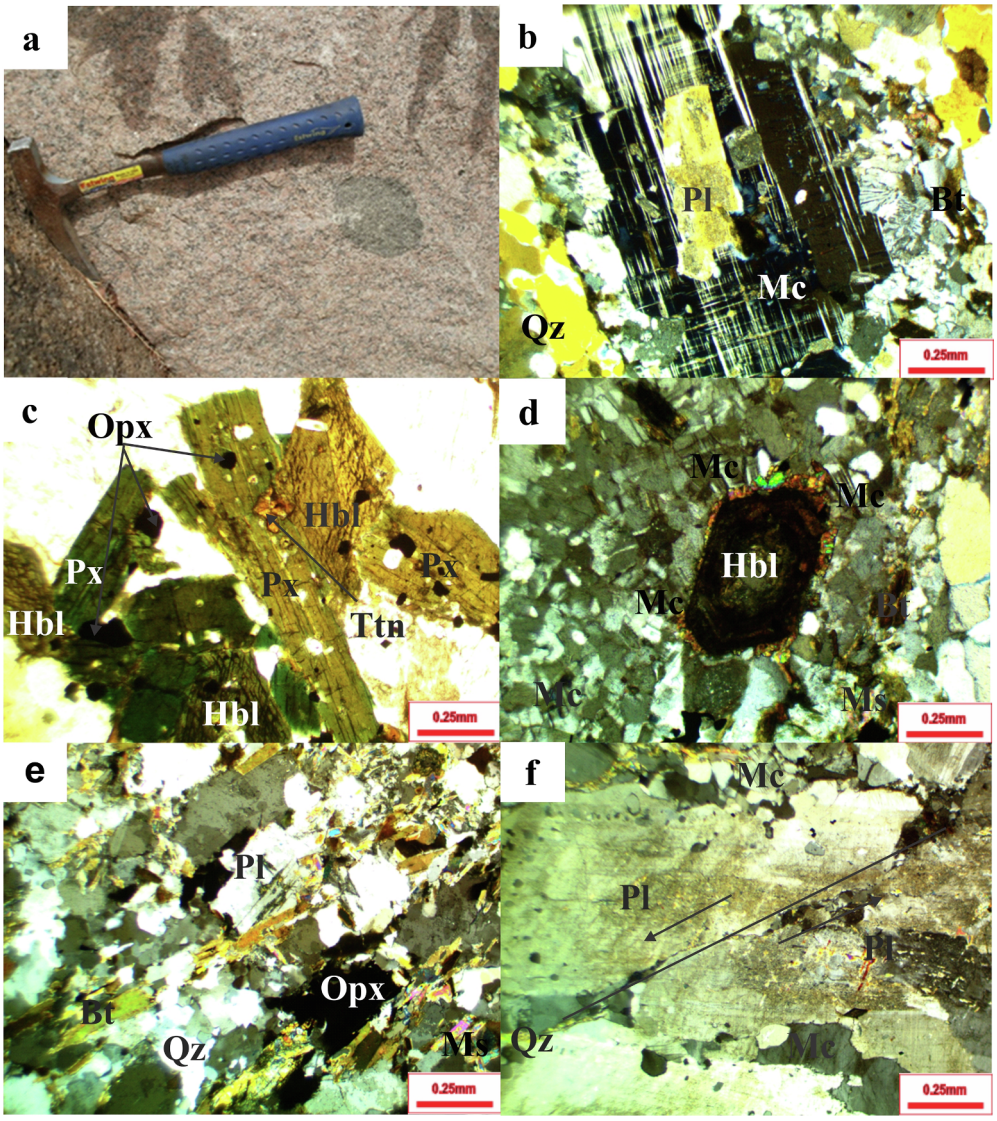

Fig. 3. (a) Representative field photograph of the studied granites. Photomicrographic features of the granites include (b) poikilitic microcline with myrmekitic associations, quartz and biotite grains; (c) elongated pyroxene and subhedral hornblende grains; (d) zoned euhedral hornblende grain with epidotized rims and interstitial chloritized biotite grains, (e) aligned grains of biotite and muscovite grains in between grains of quartz and plagioclase; (f) microfractured plagioclase grain. Photomicrographs (b), (d), (e) and (f) under crossed nicols and (c) under parallel nicols. Abbreviations: Bt (biotite), Hbl (hornblende), Mc (microcline), Ms (muscovite), Opx (opaque oxides), Pl (plagioclase), Px (pyroxene), Qz (quartz) and Ttn (titanite).

Table 1
Major phase mineral abundances (vol.%) in representative KrGs of the Bole-Nangodi belt.

Sample	Px	Hbl	Pl	Bt	Ms	K-fls	Qz
KRG							
Granite (ss)		0.1	7	7		46	40
Two-mica granite		0–1	0–28	0.01–5	0.01–5	40–80	10–50
Pyroxene granite	1–2	0–0.5	2	0.5		71–84	15–20
Hornblende granite	1	2	1–3	0–1	0.5	66–84	10–30
Meta-granite - Granitic gneiss			1–14	3–30	1–4	10–75	30–60
Granodiorite		0–0.5	20–45	4–18	0.5–2	14–25	25–55
Adamellite			27–38	4–5	0.5–1	23–32	25–40
TTG							
Trondhjemite							
Granodiorite		0–0.5	20–45	4–18	0.5–2	14–25	25–55
Pegmatite-Aplite			3		1–15	2–60	22–97

KRGs are presented in Table 4. They have SiO_2 and K_2O values in a range of 61.78–74.55 wt% (average = 70.36 wt%) and 4.17–5.49 wt% (average = 4.56 wt%) respectively. Their total alkalis ($K_2O + Na_2O$) vary from 7.87 to 9.55 wt% (average = 8.35 wt%) with Na_2O/K_2O ratios of 0.65–1.00. The KRGs have MgO, Fe_2O_3, Al_2O_3 contents and Mg# in a range of 0.34–2.57 wt% (average = 0.93 wt%), 0.87–5.97 wt% (average = 2.87 wt%), 12.96–16.29 wt% (average = 13.89 wt%) and 20.03–46.92 respectively. On the feldspar normative An-Ab-Or diagram of O'conor (1965) the KRGs plot in the granite field (not shown). They show linear trends towards A ($Na_2O + K_2O$) on the AFM diagram of Irving and Baragar (1971), indicating that the rocks are highly evolved. The KRGs belong predominantly to the high-K calc-alkaline and shoshonitic series (Fig. 8a and 8b). The rocks are mostly metaluminous to slightly peraluminous (Fig. 8d), magnesian to slightly ferroan (Fig. 8e) and plot mainly in the calc-alkaline series (Fig. 8c) and alkalic field of the MALI diagram (Fig. 8f). On the major element Harker diagrams (Fig. 9), the KRGs generally display linear trends. However, diffused patterns are observed in Na_2O vs. SiO_2 and K_2O vs. SiO_2 plots, although the latter shows a broadly linear negative correlation whereas the Al_2O_3 vs. SiO_2 plot shows two distinct trends; linear positive (from approximately 60 to 70 wt% SiO_2) and negative (from approximately 70 to 75 wt% SiO_2) (Fig. 9).

The KRGs have Sr and Y concentrations of 28.23–1443 ppm and 4.04–36.56 ppm respectively, with Sr/Y ratios of 3.30–222.8. They show strongly fractionated REE patterns (La_N/Yb_N = 5.60–224.6) on the chondrite-normalized REE diagram (Fig. 10a), with various degrees of negative Eu anomalies of 0.14–0.97 (average Eu/Eu* = 0.75). Rubidium, Ba and Th display high concentrations (Table 4) whereas Nb, Ta and Ti are depleted comparative to other elements in Early Proterozoic Upper Continental Crust (EPUCC) and Ocean Ridge Granite

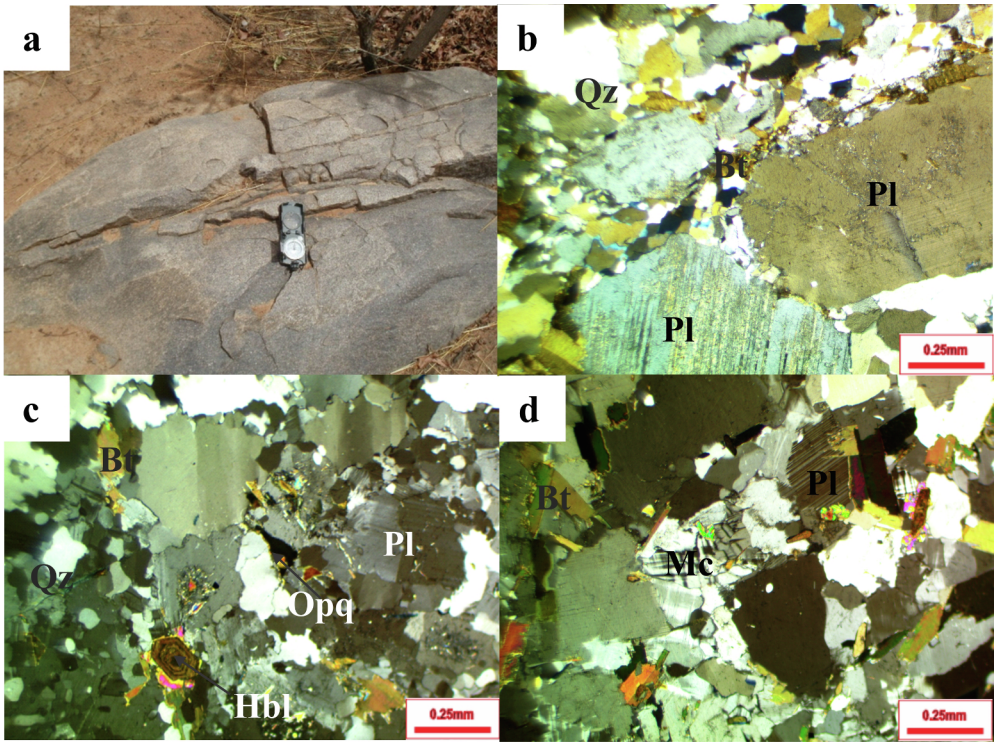

Fig. 4. (a) Representative field photograph of the studied granodiorites. Photomicrographic features of the granodiorites include (b) granulated quartz grains and sericitized plagioclase grains; (c) zoned hornblende grains with epidotized rims, sutured plagioclase grains and brecciated quartz grains; (d) biotite, microcline and plagioclase grains. All photomicrographs under crossed nicols. Abbreviations: Bt (biotite), Hbl (hornblende), Mc (microcline), Ms (muscovite), Opx (opaque oxides), Pl (plagioclase) and Qz (quartz).

Table 2
Representative electron microprobe data of selected minerals from TTGs of the Bole-Nangodi Belt.

Locality	Bongo	Du-Motigu	Funbisi		Bongo		Funbisi		Du-Motigu	Bongo		Funbisi		Du-Motigu
Sample ID	BN03A	DM03B	RA02A	RA02B	BN03A	BN03C	RA02A	RA02B	DM03B	BN03A	BN03C	RA02A	RA02B	DM03B
Mineral	Biotite				Plagioclase					K-feldspar				
	Bt-1	Bt-2	Bt-3	Bt-4	Pl-1	Pl-2	Pl-3	Pl-4	Pl-5	Fsp-1	Fsp-2	Fsp-3	Fsp-4	Fsp-5
wt.%														
SiO_2	37.63	37.46	33.15	36.59	33.03	61.79	61.92	61.42	62.65	61.80	63.08	51.96	62.36	63.33
TiO_2	1.04	1.86	2.85	2.64	0.02	0.05	0.00	0.00	0.01	0.00	0.03	0.03	0.00	0.05
Al_2O_3	14.46	15.92	14.68	16.01	21.59	23.27	22.99	22.83	18.25	17.68	18.36	15.45	18.19	18.30
Cr_2O_3	0.04	0.00	0.05	0.03	0.02	0.04	0.00	0.00	0.00	0.00	0.01	0.03	0.00	0.00
NiO	0.04	0.00	0.00	0.04	0.00	0.00	0.00	0.03	0.02	0.04	0.04	0.04	0.00	0.00
FeO	15.88	19.13	21.42	21.08	12.61	0.08	0.03	0.03	0.05	0.08	0.04	0.02	0.00	0.01
MnO	0.41	0.31	0.44	0.51	0.20	0.00	0.00	0.01	0.03	0.01	0.00	0.04	0.01	0.00
MgO	13.59	9.72	7.29	7.24	0.00	0.02	0.02	0.00	0.02	0.00	0.01	0.01	0.00	0.01
CaO	0.04	0.04	0.02	0.07	21.98	4.27	4.68	4.38	0.01	0.00	0.00	0.00	0.00	0.00
Na_2O	0.04	0.06	0.04	0.05	0.04	8.35	8.09	8.32	0.53	0.18	0.44	0.54	0.59	0.52
K_2O	9.69	9.66	9.35	9.59	0.00	0.37	0.20	0.28	15.24	15.77	15.42	14.99	15.49	15.58
P_2O_5	0.04	0.00	0.03	0.05	0.07	0.00	0.04	0.00	0.02	0.00	0.00	0.05	0.00	0.03
Total	92.89	94.16	89.31	94.33	89.54	98.25	97.98	97.30	96.81	95.56	97.43	83.14	96.64	97.85
Oxygen (24.0)														
Si	6.329	6.293	6.036	6.240	5.714	8.338	8.367	8.366	8.952	8.979	8.957	8.808	8.944	8.961
Ti	0.132	0.235	0.390	0.338	0.002	0.005	0.000	0.000	0.001	0.000	0.003	0.003	0.000	0.005
Al	2.867	3.152	3.149	3.218	4.402	3.701	3.662	3.665	3.074	3.027	3.074	3.086	3.075	3.052
Cr	0.005	0.000	0.007	0.005	0.002	0.004	0.000	0.000	0.000	0.000	0.002	0.004	0.000	0.000
Ni	0.006	0.000	0.000	0.005	0.000	0.000	0.000	0.003	0.002	0.004	0.004	0.005	0.000	0.000
Fe	2.234	2.687	3.262	3.008	1.824	0.009	0.003	0.004	0.006	0.009	0.005	0.002	0.000	0.002
Mn	0.058	0.045	0.068	0.074	0.029	0.000	0.000	0.002	0.003	0.001	0.000	0.006	0.001	0.000
Mg	3.407	2.435	1.978	1.839	0.000	0.004	0.004	0.000	0.003	0.000	0.001	0.002	0.000	0.001
Ca	0.007	0.007	0.005	0.013	4.074	0.618	0.678	0.639	0.001	0.000	0.000	0.000	0.000	0.000
F	0.014	0.018	0.013	0.017	0.014	2.186	2.120	2.197	0.146	0.051	0.122	0.177	0.163	0.144
Na	2.078	2.071	2.171	2.087	0.001	0.063	0.035	0.048	2.778	2.923	2.793	3.241	2.835	2.812
Cl	0.005	0.000	0.004	0.007	0.010	0.000	0.004	0.000	0.003	0.000	0.000	0.007	0.000	0.004
K	0.366	0.000	0.155	0.399	0.000	0.006	0.008	0.000	0.000	0.000	0.000	0.000	0.000	0.008
P	0.002	0.004	0.003	0.000	0.007	0.000	0.000	0.000	0.000	0.000	0.003	0.001	0.001	0.001

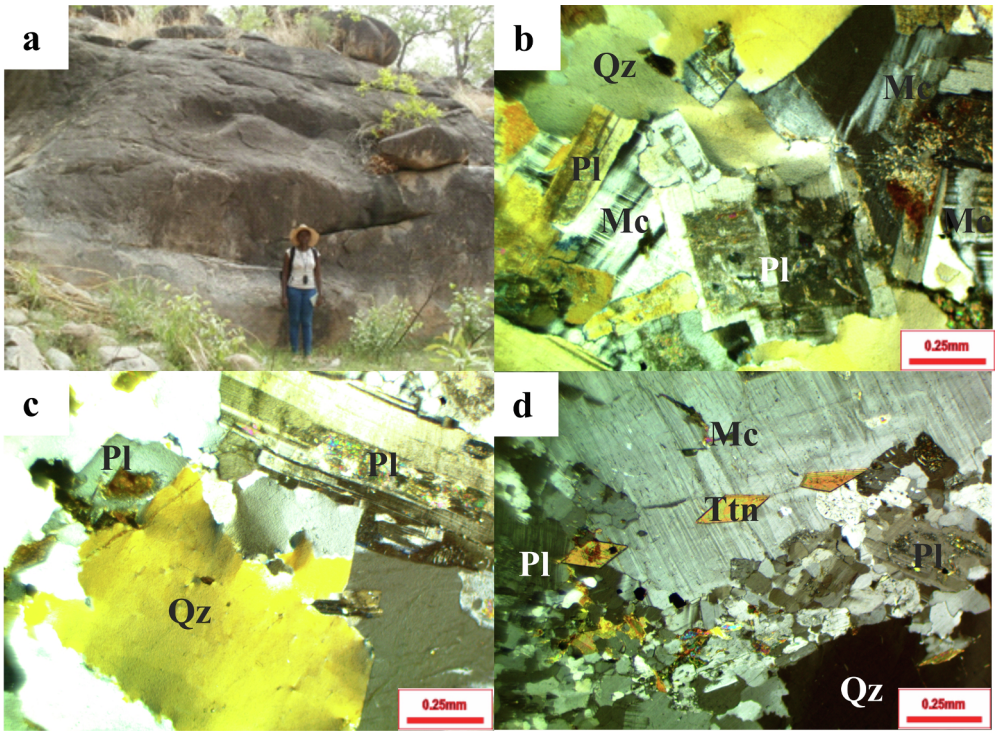

Fig. 5. (a) Representative field photograph of the studied adamellites. Photomicrographic features of the adamellites include (b) recrystallized plagioclase grains, and microcline and quartz grains; (c); quartz and sericitized plagioclase grains; (d) aligned titanite grains within microcline grains and altered plagioclase cores. All photomicrographs under crossed nicols. Abbreviations: Bt (biotite), Mc (microcline), Ms (muscovite), Pl (plagioclase), Qz (quartz) and Ttn (Titanite).

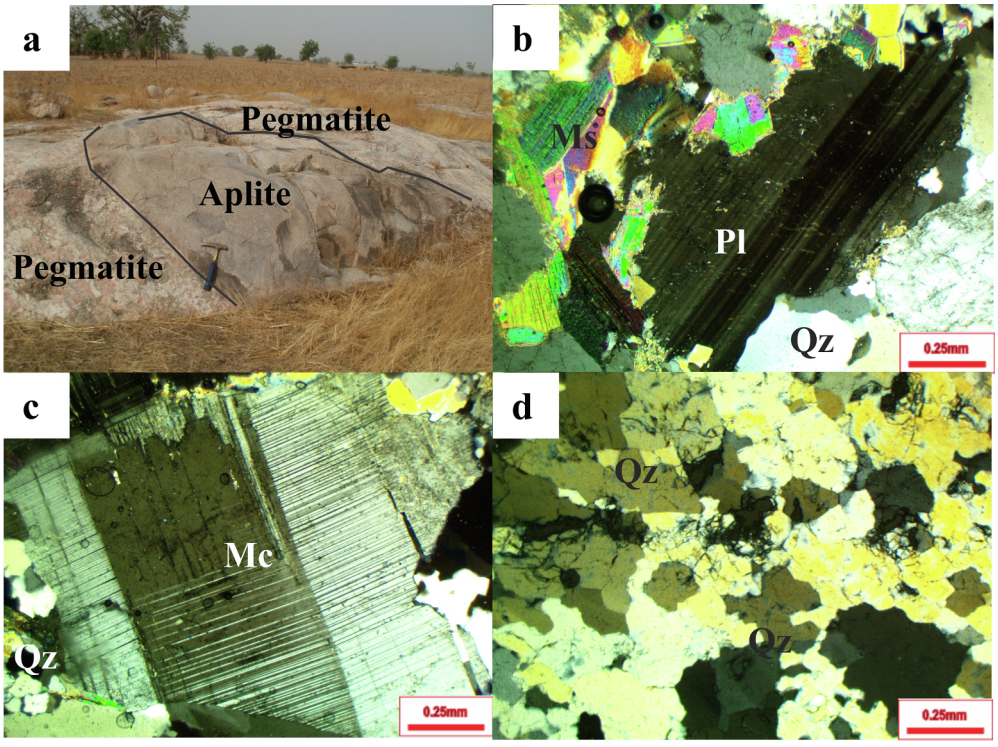

Fig. 6. (a) Representative field photograph of the studied pegmatite/aplite associations. Photomicrographic features of the pegmatite/aplite associations (b, c and d) include plagioclase, muscovite, microcline and quartz grains, all under crossed nicols. Abbreviations: Mc (microcline), Ms (muscovite), Pl (plagioclase) and Qz (quartz).

(ORG) normalized multi-element diagrams (Fig. 10b and 10c).

4.2.2. TTG

Results of whole-rock major and trace elements analyse of the TTGs are presented in Table 4. They have SiO_2 and K_2O values in a range of 65.57–75.63 wt% (average = 69.47 wt%) and 1.31–3.86 wt% (average = 2.96 wt%) respectively. Their total alkalis ($K_2O + Na_2O$) vary from 5.21 to 8.41 wt% (average = 7.40 wt%) resulting in Na_2O/K_2O ratios of 1.04–2.98. The TTGs have MgO, Fe_2O_3, and Al_2O_3 contents of 0.70–1.80 wt% (average = 1.07 wt%), 2.86–4.13 wt% (average = 3.27 wt%), 12.72–15.47 wt% (average = 14.39 wt%) respectively and Mg# of 28.44–46.33. On the feldspar normative An-Ab-Or diagram of O'conor (1965), the TTGs plot mainly in the trondhjemite field with few straddling the trondhjemite and granite boundary (not shown). On the AFM diagram of Irving and Baragar (1971) the TTGs display only slight evolution when compared with the KRGs. The TTGs also plot mainly in the field defined by high-K calc-alkaline and shoshonitic series (Fig. 8a and Fig. 8b). They are mostly metaluminous

Table 3
Representative electron microprobe data of selected minerals from KRGs of the Bole-Nangodi Belt.

Locality	Tongo	Chaqpaala	Du-Motigu	Bongo		Bongo			Tongo		Funbisi			Naga
Sample ID	TG01C	ZK01	DM03A	BS04	BN02	BN02	BN03C	BS04	TG01C	TG01G	RA03B	RA06	RA08	NB01A
Mineral	Pyroxene		Hornblende			Biotite								
	Px-1	Px-2	Hbl-1	Hbl-2	Hbl-3	Bt-1	Bt-2	Bt-3	Bt-4	Bt-5	Bt-5	Bt-6	Bt-7	Bt-8
wt.%														
SiO_2	26.61	29.07	35.83	45.48	47.59	36.80	36.69	39.74	33.16	36.93	35.26	35.90	36.27	39.34
TiO_2	0.00	0.14	0.53	0.49	0.86	0.75	1.64	0.71	1.13	1.58	5.61	2.72	3.09	1.23
Al_2O_3	19.23	17.47	9.04	7.11	6.16	12.47	14.63	12.71	12.07	14.63	15.29	16.81	16.78	14.52
Cr_2O_3	0.03	0.04	0.02	0.02	0.01	0.02	0.01	0.07	0.02	0.02	0.08	0.05	0.03	0.00
NiO	0.02	0.03	0.00	0.00	0.03	0.00	0.00	0.02	0.00	0.01	0.00	0.02	0.04	0.03
FeO	21.78	15.82	20.46	17.62	15.66	13.81	17.82	14.43	13.84	16.38	23.33	23.09	23.67	16.91
MnO	1.01	0.55	0.50	0.47	0.50	0.48	0.34	0.37	0.41	0.59	0.33	0.40	0.32	0.52
MgO	16.88	20.59	8.28	11.25	12.76	15.63	12.25	16.01	13.24	11.79	5.59	6.11	5.97	10.77
CaO	0.05	0.13	11.33	11.02	11.30	0.04	0.06	0.02	0.05	0.05	1.69	0.13	0.02	0.01
Na_2O	0.00	0.01	1.38	1.61	1.78	0.09	0.04	0.04	0.03	0.05	0.05	0.03	0.04	0.00
K_2O	0.01	0.57	1.42	1.12	0.79	9.80	9.56	9.74	9.59	9.60	7.93	9.14	9.56	9.87
P_2O_5	0.00	0.03	0.04	0.03	0.00	0.00	0.00	0.00	0.01	0.04	0.00	0.01	0.00	0.04
Total	85.61	84.44	88.83	96.24	97.44	89.87	93.02	93.86	83.55	92.02	95.15	94.40	96.04	93.62
Oxygen (24.0)														
Si	4.854	5.196	6.475	7.261	7.404	6.380	6.229	6.549	6.254	6.321	5.997	6.135	6.129	6.591
Ti	0.000	0.019	0.072	0.059	0.101	0.097	0.209	0.088	0.160	0.204	0.717	0.349	0.393	0.155
Al	4.134	3.680	1.926	1.338	1.130	2.548	2.929	2.468	2.683	2.951	3.065	3.387	3.342	2.867
Cr	0.004	0.005	0.003	0.002	0.001	0.003	0.002	0.009	0.004	0.003	0.010	0.007	0.004	0.000
Ni	0.002	0.004	0.000	0.000	0.004	0.000	0.000	0.003	0.000	0.002	0.000	0.003	0.006	0.004
Fe	3.323	2.365	3.092	2.353	2.037	2.003	2.530	1.989	2.183	2.345	3.319	3.300	3.345	2.370
Mn	0.156	0.083	0.077	0.064	0.065	0.071	0.048	0.051	0.065	0.086	0.047	0.057	0.046	0.074
Mg	4.591	5.485	2.230	2.677	2.958	4.040	3.100	3.933	3.722	3.009	1.417	1.557	1.503	2.691
Ca	0.011	0.025	2.194	1.885	1.883	0.007	0.010	0.004	0.011	0.009	0.308	0.023	0.004	0.001
F	0.000	0.002	0.483	0.498	0.537	0.029	0.013	0.014	0.010	0.016	0.015	0.010	0.012	0.000
Na	0.002	0.131	0.327	0.228	0.157	2.167	2.070	2.048	2.308	2.096	1.721	1.993	2.062	2.109
Cl	0.000	0.005	0.006	0.004	0.000	0.000	0.000	0.000	0.001	0.005	0.000	0.001	0.000	0.005
K	0.000	0.000	0.000	0.028	0.018	0.618	0.447	0.707	0.729	0.325	0.251	0.130	0.240	0.348
P	0.001	0.001	0.001	0.000	0.001	0.002	0.000	0.000	0.005	0.000	0.000	0.003	0.001	0.003

Locality	Chaqpaala			Du-Motigu	Bongo			Tongo		Funbisi			Naga	Chaqpaala	
Sample ID	ZK05	ZK07	ZK08	DM03A	BN01	BN02	BS04	TG01G	TG01C	RA03B	RA06	RA08	NB01A	ZK01	ZK05
Mineral	Biotite				Plagioclase										
	Bt-10	Bt-11	Bt-13	Bt-14	Pl-1	Pl-2	Pl-3	Pl-4	Pl-5	Pl-6	Pl-7	Pl-8	Pl-9	Pl-10	Pl-11
wt.%															
SiO_2	34.88	36.88	36.21	36.94	65.13	36.48	63.98	63.95	64.07	62.96	65.93	64.29	37.21	64.29	63.94
TiO_2	1.63	1.89	1.65	1.51	0.00	0.01	0.00	0.00	0.00	0.00	0.02	0.02	0.02	0.00	0.03
Al_2O_3	15.03	15.03	15.55	15.68	20.95	20.46	21.31	21.60	20.58	21.64	20.43	21.64	22.94	20.96	21.50
Cr_2O_3	0.08	0.07	0.06	0.04	0.02	0.00	0.00	0.00	0.00	0.00	0.02	0.02	0.03	0.00	0.00
NiO	0.00	0.04	0.00	0.01	0.00	0.00	0.01	0.00	0.01	0.00	0.00	0.00	0.01	0.00	0.00
FeO	18.91	19.36	18.23	18.91	0.05	14.09	0.11	0.10	0.14	0.00	0.04	0.00	11.55	0.00	0.05
MnO	0.42	0.38	0.61	0.29	0.00	0.19	0.00	0.01	0.00	0.01	0.00	0.00	0.52	0.00	0.01
MgO	10.28	10.82	11.53	11.16	0.00	0.01	0.00	0.02	0.04	0.01	0.00	0.00	0.00	0.01	0.00
CaO	0.07	0.09	0.07	0.02	1.75	22.68	2.73	3.03	2.45	3.41	1.61	3.17	22.51	2.53	2.83
Na_2O	0.06	0.04	0.07	0.04	9.87	0.00	9.35	9.48	9.74	8.80	10.22	9.27	0.01	9.63	9.30
K_2O	9.61	9.75	9.42	9.34	0.13	0.00	0.09	0.13	0.27	0.29	0.05	0.19	0.01	0.05	0.19
P_2O_5	0.01	0.03	0.00	0.00	0.00	0.01	0.02	0.00	0.02	0.00	0.00	0.00	0.00	0.00	0.07
Total	90.99	94.36	93.39	93.93	97.91	93.92	97.59	98.32	97.31	97.12	98.33	98.61	94.78	97.47	97.93
Oxygen (24.0)															
Si	6.126	6.218	6.139	6.216	8.737	6.021	8.635	8.588	8.689	8.558	8.802	8.601	5.983	8.682	8.607
Ti	0.215	0.240	0.210	0.192	0.000	0.001	0.000	0.000	0.000	0.000	0.002	0.002	0.002	0.000	0.003
Al	3.112	2.988	3.108	3.109	3.313	3.980	3.390	3.419	3.289	3.467	3.216	3.412	4.348	3.337	3.411
Cr	0.011	0.009	0.008	0.005	0.003	0.000	0.000	0.000	0.000	0.000	0.002	0.003	0.004	0.000	0.000
Ni	0.000	0.005	0.000	0.002	0.000	0.000	0.001	0.000	0.001	0.000	0.000	0.000	0.001	0.000	0.000
Fe	2.777	2.730	2.585	2.661	0.006	1.944	0.013	0.012	0.016	0.000	0.005	0.000	1.553	0.000	0.006
Mn	0.062	0.055	0.087	0.041	0.000	0.027	0.000	0.001	0.000	0.001	0.000	0.000	0.070	0.000	0.001
Mg	2.692	2.719	2.915	2.798	0.000	0.002	0.000	0.003	0.008	0.001	0.000	0.001	0.000	0.002	0.000
Ca	0.014	0.016	0.013	0.004	0.252	4.010	0.395	0.436	0.356	0.496	0.231	0.454	3.879	0.365	0.408
F	0.020	0.014	0.021	0.013	2.568	0.001	2.446	2.468	2.560	2.319	2.646	2.405	0.002	2.521	2.428
Na	2.154	2.097	2.036	2.005	0.022	0.000	0.016	0.022	0.048	0.051	0.008	0.033	0.002	0.008	0.033
Cl	0.001	0.004	0.000	0.000	0.000	0.001	0.002	0.000	0.002	0.000	0.000	0.000	0.000	0.000	0.008
K	0.000	0.000	0.000	0.000	0.000	0.000	0.000	0.0047	0.011	0.000	0.000	0.003	0.000	0.000	0.007
P	0.005	0.000	0.000	0.000	0.000	0.000	0.002	0.0032	0.004	0.000	0.005	0.000	0.000	0.000	0.001

Locality	Chaqpaala		Du-Motigu	Bongo			Funbisi			Tongo		Naga	Chaqpaala		
Sample ID	ZK07	ZK08	DM03A	BN01	BN02	BS04	RA03B	RA06	RA08	TG01G	TG01C	NB01A	ZK01	ZK05	ZK07
Mineral	Plagioclase			K-feldspar											

(*continued on next page*)

Table 3 (*continued*)

Locality	Chaqpaala		Du-Motigu	Bongo			Funbisi			Tongo		Naga	Chaqpaala		
Sample ID	ZK07	ZK08	DM03A	BN01	BN02	BS04	RA03B	RA06	RA08	TG01G	TG01C	NB01A	ZK01	ZK05	ZK07
	Pl-12	Pl-13	Pl-14	Fsp-1	Fsp-2	Fsp-3	Fsp-4	Fsp-5	Fsp-6	Fsp-7	Fsp-8	Fsp-9	Fsp-10	Fsp-11	Fsp-12
wt.%															
SiO_2	59.83	62.13	61.04	63.50	63.06	63.44	63.22	63.54	63.86	63.74	64.07	63.97	63.07	63.09	62.94
TiO_2	0.00	0.01	0.01	0.05	0.00	0.04	0.01	0.00	0.02	0.02	0.00	0.00	0.00	0.00	0.02
Al_2O_3	20.70	21.33	21.38	18.07	18.07	18.22	17.91	18.28	18.36	18.09	20.58	18.04	17.86	18.37	17.74
Cr_2O_3	0.03	0.00	0.09	0.00	0.00	0.00	0.00	0.00	0.00	0.01	0.00	0.04	0.01	0.00	0.04
NiO	0.01	0.00	0.00	0.01	0.00	0.00	0.04	0.00	0.04	0.00	0.01	0.00	0.05	0.02	0.00
FeO	0.13	0.07	0.08	0.05	0.05	0.11	0.03	0.01	0.02	0.07	0.14	0.02	0.05	0.13	0.07
MnO	0.05	0.00	0.00	0.01	0.02	0.00	0.00	0.00	0.00	0.02	0.00	0.00	0.01	0.00	0.01
MgO	0.02	0.02	0.05	0.00	0.02	0.01	0.00	0.00	0.00	0.01	0.04	0.02	0.01	0.00	0.03
CaO	1.11	2.77	3.52	0.00	0.00	0.02	0.03	0.00	0.00	0.02	2.45	0.00	0.00	0.03	0.06
Na_2O	9.02	9.35	8.31	0.63	0.23	0.40	0.68	0.42	0.56	0.48	9.74	0.25	0.55	0.46	0.20
K_2O	1.23	0.10	0.21	15.31	15.81	15.57	15.65	15.96	15.71	15.96	0.27	16.07	15.61	15.76	16.07
P_2O_5	0.03	0.00	0.00	0.00	0.00	0.00	0.07	0.00	0.01	0.00	0.02	0.03	0.00	0.00	0.05
Total	92.15	95.78	94.70	97.63	97.25	97.82	97.63	98.21	98.58	98.42	97.34	98.43	97.22	97.87	97.22
Oxygen (24.0)															
Si	8.585	8.561	8.511	8.993	8.984	8.976	8.978	8.971	8.971	8.985	8.689	9.006	8.993	8.943	8.990
Ti	0.000	0.001	0.001	0.005	0.000	0.004	0.001	0.000	0.002	0.002	0.000	0.000	0.000	0.000	0.002
Al	3.502	3.465	3.514	3.017	3.035	3.039	2.998	3.041	3.041	3.006	3.289	2.993	3.002	3.069	2.986
Cr	0.003	0.000	0.010	0.000	0.000	0.000	0.000	0.000	0.000	0.001	0.000	0.004	0.001	0.000	0.004
Ni	0.001	0.000	0.000	0.001	0.000	0.000	0.004	0.000	0.004	0.000	0.001	0.000	0.006	0.002	0.000
Fe	0.015	0.009	0.010	0.006	0.006	0.013	0.003	0.002	0.002	0.008	0.016	0.002	0.006	0.016	0.008
Mn	0.006	0.000	0.000	0.001	0.003	0.000	0.000	0.000	0.000	0.002	0.000	0.000	0.001	0.000	0.002
Mg	0.005	0.004	0.011	0.000	0.003	0.003	0.000	0.000	0.000	0.002	0.008	0.003	0.002	0.000	0.007
Ca	0.171	0.410	0.527	0.000	0.000	0.003	0.004	0.000	0.001	0.003	0.356	0.000	0.000	0.004	0.009
F	2.509	2.498	2.247	0.173	0.062	0.111	0.186	0.116	0.154	0.007	2.560	0.069	0.151	0.126	0.056
Na	0.225	0.017	0.037	2.766	2.873	2.811	2.836	2.875	2.816	0.131	0.048	2.886	2.839	2.851	2.929
Cl	0.004	0.000	0.000	0.000	0.000	0.000	0.009	0.000	0.001	0.000	0.002	0.004	0.000	0.000	0.006
K	0.000	0.000	0.000	0.000	0.010	0.000	0.000	0.007	0.000	2.871	0.011	0.000	0.000	0.009	0.004
P	0.001	0.000	0.000	0.000	0.004	0.000	0.000	0.006	0.000	0.000	0.004	0.000	0.002	0.001	0.000

to slightly peraluminous (Fig. 8d), mainly magnesian (Fig. 8e) and plot in the calc-alkaline series (Fig. 8c) and the calc-alkalic to alkalic fields of the MALI diagram (Fig. 8f). On the major element Harker diagrams, the KRGs display linear trends. However, diffused patterns are observed in Na_2O and K_2O vs SiO_2 plots (Fig. 9).

The TTGs have Sr and Y concentrations of 614–1245 ppm, 5.09–12.10 ppm respectively and Sr/Y ratios of 31.8–140.1 They show strongly fractionated REE patterns (La_N/Yb_N = 32.3–82.8) on the chondrite-normalized REE diagram (Fig. 10a), with slightly negative to almost no Eu anomalies of 0.81–1.01 (average Eu/Eu* = 0.86). Barium, Rb and Th display high concentrations whereas Nb, Ta and Ti are depleted compared to other elements in Early Proterozoic Upper Continental Crust (EPUCC) and Ocean Ridge Granite (ORG) normalized multi-element diagrams (Fig. 10b and 10c).

4.2.3. Pegmatite and aplite

Only one sample each of the pegmatite and aplite were analyzed for whole-rock major and trace element composition (Table 4). Their SiO_2 and K_2O values are 76.16 and 81.89 wt%, and 1.77 and 2.26 wt% respectively, whereas their total alkalis ($K_2O + Na_2O$) are 4.81 and 6.72 wt% with Na_2O/K_2O values of 1.72 and 1.97 respectively. The have MgO, Fe_2O_3, and Al_2O_3 contents of 0.15 and 0.16 wt%, 1.15 and 1.32 wt%, and 10.97 and 14.19 wt%, and Mg# of 19.36–20.53 respectively. On the AFM diagram of Irving and Baragar (1971) they show characteristics of highly evolved rocks. The pegmatite and aplite are calc-alkaline (Fig. 8a–c), peraluminous (Fig. 8d) and ferroan (Fig. 8e) in composition. On the major element Harker diagrams, the rocks display linear trends with the exception of MgO vs. SiO_2 and P_2O_5 vs. SiO_2 where they appear static (Fig. 9).

The pegmatite and aplite have Sr and Y concentrations of 37.5 and 20.8 ppm, and 14.5 and 16.4 ppm respectively, with corresponding Sr/Y ratios of 2.59 and 1.27. They show weakly fractionated REE patterns (La_N/Yb_N = 1.8 and 0.9) on the chondrite normalized REE diagram (Fig. 10a), with negative Eu anomalies of 0.40 and 0.18 respectively. Rubidium, Nb, Ta and Ti (averagely high) display high concentrations relative to KRGs and TTGs and depleted Ba and Th compared to other elements in Early Proterozoic Upper Continental Crust (EPUCC) and Ocean Ridge Granite (ORG) normalized multi-element diagrams (Fig. 10b and 10c).

4.3. Strontium (Sr)-neodymium (Nd) isotope geochemistry

Strontium-neodymium isotopic compositions of the studied samples are presented in Table 5. $^{87}Sr/^{86}Sr$ and $^{143}Nd/^{144}Nd$ ratios for the KRGs range from 0.7097 to 0.8133 and 0.5109 to 0.5113 respectively, whereas those for the TTGs are 0.7091–0.7185 and 0.5111–0.5112 respectively. The samples display strongly fractionated $^{147}Sm/^{144}Nd$ ratios (0.0711–0.1030 and 0.0808–0.0893 respectively). The initial $^{87}Sr/^{86}Sr$ (I_{Sr}) values calculated for the KRGs and TTGs at 2.1 Ga, which represents the crustal formation age during the Eburnean orogeny (e.g., Abouchami et al., 1990; Boher et al., 1992) are generally variable (0.6021–0.7320 and 0.6491–0.6687 respectively), whereas their $\varepsilon_{Nd}(t)$ range from −0.86 to + 1.37 and + 0.90 to + 1.24 respectively. The crustal residence ages of the TTGs and KRGs calculated according to the depleted mantle model ages of DePaolo (1998) are T_{DM1} (2.34–2.38 Ga and 2.36–2.53 Ga respectively) and T_{DM2} (2.21–2.24 Ga and 2.22–2.39 Ga respectively). However, the T_{DM2} ages appear to be very consistent and generally close to the formation age of 2.1 Ga. A generally negative correlation trend is highlighted in the $\varepsilon_{Nd}(t)$ vs. $(^{87}Sr/^{86}Sr)_i$ plots where samples mainly show affinity for the mantle array (Fig. 11a), particularly the HIMU (Fig. 11b).

5. Discussion

5.1. Alteration and effects of weathering

The loss on ignition (LOI) values for the studied rocks are in the range of 0.00–1.06 % (average 0.47%) (Table 4). These values are significantly low, suggestive of the relatively fresh nature of the samples. Several previous studies have revealed that the Birimian rocks

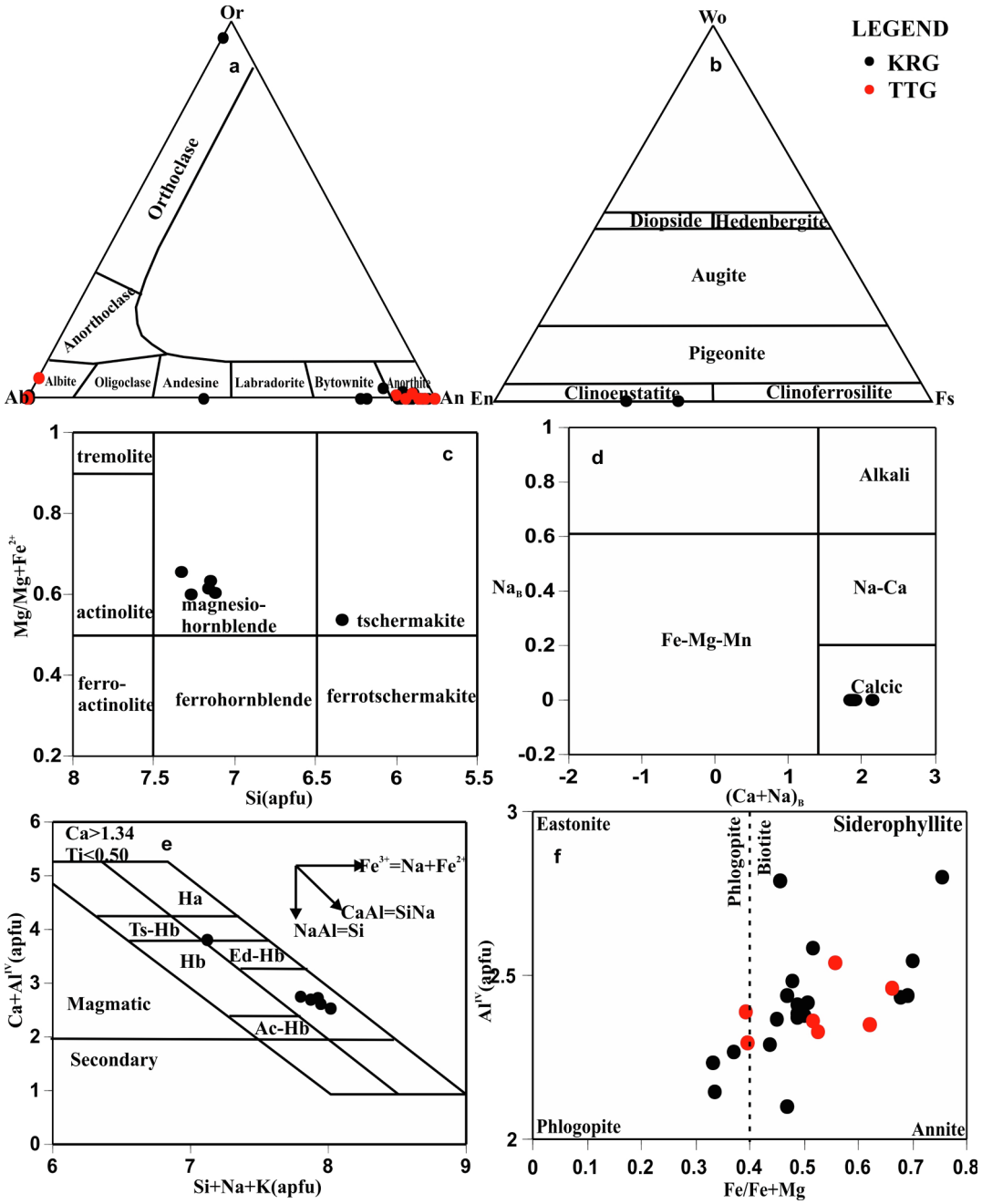

Fig. 7. (a) Or-Ab-An ternary diagram (Deer et al., 1992); (b) Wo-En-Fs ternary diagram (Lindsley, 1983); (c) Mg/Mg + Fe^{2+} vs. Si classification diagram (Leake et al., 1997); (d) Na_B vs. $[Ca + Na]_B$ diagram (Leake et al., 1997). (e) Ca + Al^{IV} vs. Si + Na + K diagram (Giret et al., 1980). (f) Al^{IV} vs. Fe/Fe + Mg diagram (Deer et al., 1992).

have been metamorphosed mostly under greenschist facies conditions (e.g. Leube et al., 1990; Sylvester and Attoh, 1992; Dampare et al., 2008; Amponsah et al., 2015, 2016; Block et al., 2016a). From petrographic studies of the granitoids, evidence from the primary mineral assemblages and textures suggest that they have not been extensively altered. That notwithstanding, chemical index of alteration (CIA) (Nesbitt and Young, 1982) was calculated for the granitoids to determine the extent to which they have been altered by secondary processes. The CIA values obtained are 41.6–51.5 with an average value of 49.2 for the KRGs, 48.8–52.3 with an average of 49.8 for the TTGs, 56.0 for the pegmatite and 58.7 for the aplite. According to Nesbitt and Young (1982), CIA value of unaltered granitoids is 50, and any CIA value exceeding 60 can be considered as significantly altered. The range of values suggests our samples are relatively fresh, with minor alteration, and therefore, they could be relied upon for geochemical investigations. Similarly, The calc-alkaline to high-K calc-alkaline and shoshonite series affinity commonly displayed by the granitoids on the plots of transition vs. fluid immobile elements (e.g. Co vs. Th; Fig. 8a; Hastie et al., 2007) and K_2O vs. SiO_2 (Fig. 8b; Peccerillo and Taylor, 1976) indicate that the LILE (e.g. K) were least affected by alteration and/or metamorphism. Thus, even though the alkalis (e.g. K_2O and Na_2O) values may have been affected by alteration, the LOI and CIA values and inferences made from them strongly indicate they are relatively primary.

5.2. Temperature-Pressure conditions of crystallization

Biotites and hornblendes are the most dominant mafic minerals in

Table 4
Whole-rock major and trace element data of representative KRGs, TTGs, pegmatite-aplite rocks of the Bole Nangodi belt.

Rock type	KRGs														
	Granite (s.s.)		Two-mica granite												
Locality	Funbisi	Tongo	Funbisi					Bongo		Du-Motigu		Naga	Tongo		
Sample ID	RA01	TG01G	RA03A	RA03D	RA04	RA05	RA06	BN01	BN02	DM02	DM03A	NB01A	TG01B	TG01F	TG01H
wt.%															
SiO_2	71.37	69.50	74.36	74.20	74.46	74.18	74.55	70.35	67.80	73.54	64.93	72.70	69.18	69.03	69.59
TiO_2	0.57	0.47	0.22	0.22	0.25	0.23	0.24	0.34	0.66	0.06	0.72	0.20	0.50	0.45	0.47
Al2O3	13.78	14.18	13.77	13.86	13.37	13.12	13.31	14.78	13.89	15.49	16.29	13.78	14.01	14.10	14.11
Fe_2O_{3T}	3.03	3.12	1.81	1.80	2.01	1.84	1.88	1.58	3.77	0.87	3.20	1.82	3.37	3.06	2.89
MnO	0.07	0.07	0.06	0.05	0.05	0.05	0.05	0.04	0.07	0.04	0.05	0.07	0.08	0.07	0.07
MgO	0.73	1.02	0.34	0.36	0.41	0.36	0.37	0.29	1.24	0.11	1.24	0.46	1.11	0.97	0.99
CaO	1.48	2.03	1.14	1.14	1.07	1.10	1.04	1.07	2.57	0.76	3.03	1.23	2.02	1.88	2.08
Na_2O	3.44	3.98	3.54	3.54	3.29	3.39	3.33	4.06	3.90	4.19	4.36	4.31	4.00	4.00	4.02
K_2O	4.64	4.50	4.78	4.84	4.87	4.50	4.81	5.49	4.63	4.50	4.41	4.18	4.46	4.50	4.35
P_2O5	0.15	0.23	0.06	0.06	0.07	0.07	0.07	0.07	0.32	0.05	0.37	0.10	0.23	0.23	0.22
LOI (%)	0.30	0.52	0.22	0.24	0.26	0.26	0.20	0.42	0.54	0.66	0.00	0.62	0.60	0.54	0.60
TOTAL	99.56	99.62	100.30	100.31	100.11	99.10	99.85	98.49	99.39	100.27	98.60	99.47	99.56	98.83	99.39
K_2O/Na_2O	1.35	1.13	1.35	1.37	1.48	1.33	1.44	1.35	1.19	1.07	1.01	0.97	1.12	1.13	1.08
$K_2O + Na_2O$	8.08	8.48	8.32	8.38	8.16	7.89	8.14	9.55	8.53	8.69	8.77	8.49	8.46	8.50	8.37
Mg#	32.31	39.31	27.12	28.38	28.78	27.93	28.05	26.67	39.45	32.03	43.43	33.36	39.49	38.57	40.43
A/CNK	1.03	0.94	1.05	1.06	1.06	1.05	1.06	1.01	0.86	1.18	0.93	0.99	0.93	0.95	0.93
A/NK	1.29	1.24	1.25	1.25	1.25	1.26	1.25	1.17	1.22	1.32	1.36	1.19	1.23	1.23	1.25
ppm															
Sc	4.29	4.86	2.86	2.79	3.21	3.27	3.04	1.91	5.83	3.04	5.63	3.09	4.80	4.44	5.44
V	31.56	40.79	16.12	16.04	17.64	16.74	17.19	17.62	50.51	4.48	55.72	19.74	43.50	35.68	39.96
Cr	39.94	40.12	43.12	45.25	28.96	47.51	36.82	18.88	47.33	16.83	24.83	33.95	50.77	37.03	37.67
Co	5.04	5.91	2.31	2.40	2.39	2.65	2.44	1.55	7.23	0.50	8.26	2.74	6.34	5.18	5.82
Ni	45.63	15.55	61.42	49.91	25.24	45.83	26.24	14.17	25.59	6.36	35.83	14.62	19.98	13.38	31.93
Cu	21.61	10.20	26.23	20.62	84.09	18.17	12.83	11.38	20.55	3.68	12.36	7.23	11.80	19.28	21.21
Zn	78.63	58.01	39.05	41.55	56.18	52.14	47.76	31.68	72.35	45.09	65.81	50.21	67.48	55.62	65.00
Ga	21.71	22.14	21.13	22.44	20.19	21.01	21.67	18.09	20.35	33.32	22.59	24.99	22.14	20.08	22.24
Rb	214	162	204	207	205	214	211	174	182	323	64.11	166	148	142	155
Sr	361	706	162	161	154	159	152	1268	1058	28.29	1060	514	641	626	755
Zr	392	169	122	124	120	105	131	202	351	25.30	227	140	174	170	238
Nb	8.96	7.16	9.09	8.66	8.53	8.66	11.42	5.92	11.35	15.12	7.57	8.37	8.18	6.18	7.63
Cs	13.83	11.58	4.04	4.04	3.41	4.74	4.26	14.67	11.89	11.63	4.82	5.17	16.87	11.48	11.12
Ba	2157	1225	799	817	825	801	850	3002	1629	29.06	1700	899	1102	1109	1226
La	103	37.07	45.16	132	41.63	37.83	38.15	56.03	84.16	4.91	54.44	26.42	45.00	38.52	44.62
Ce	182	79.24	81.36	229	75.44	69.53	69.61	97.09	173	9.70	113	49.65	89.53	78.32	93.49
Pr	18.61	9.97	8.66	22.73	8.09	7.46	7.51	11.87	20.61	1.29	13.85	6.50	10.81	9.31	11.45
Nd	61.77	38.52	27.82	72.74	25.93	24.21	24.29	37.20	74.04	4.86	49.58	23.41	37.47	31.79	43.40
Sm	7.25	6.11	3.66	8.76	3.38	3.40	3.36	5.00	12.35	1.44	8.31	3.45	5.99	5.37	6.74
Eu	1.15	1.35	0.61	0.77	0.63	0.62	0.63	1.14	2.69	0.07	2.02	0.90	1.35	1.17	1.52
Gd	4.56	3.94	2.50	5.74	2.20	2.23	2.33	2.89	8.36	1.50	5.38	2.35	4.03	3.41	4.45
Tb	0.43	0.42	0.26	0.54	0.23	0.23	0.27	0.28	0.92	0.27	0.58	0.27	0.44	0.36	0.48
Dy	1.53	1.63	0.95	1.74	0.86	0.82	1.01	1.19	3.86	1.55	2.27	1.07	1.72	1.53	1.95
Ho	0.26	0.28	0.15	0.25	0.14	0.13	0.16	0.19	0.65	0.29	0.37	0.19	0.30	0.24	0.33
Er	0.63	0.69	0.38	0.54	0.39	0.35	0.43	0.49	1.59	0.70	0.87	0.51	0.76	0.63	0.83
Tm	0.09	0.10	0.05	0.06	0.06	0.05	0.06	0.07	0.22	0.10	0.11	0.08	0.10	0.09	0.12
Yb	0.57	0.63	0.33	0.37	0.39	0.35	0.40	0.48	1.43	0.59	0.67	0.56	0.68	0.55	0.74
Lu	0.09	0.10	0.05	0.05	0.06	0.05	0.06	0.07	0.22	0.08	0.09	0.10	0.11	0.09	0.12
Y	6.96	8.09	4.42	6.62	4.46	4.04	4.99	5.69	18.37	8.57	9.80	6.19	8.64	7.05	9.49
Hf	9.60	5.84	4.28	4.38	4.18	3.65	4.71	5.84	10.05	1.62	6.21	6.05	6.28	5.47	7.65
Ta	0.75	0.53	0.89	0.82	0.86	0.87	1.04	0.60	1.11	1.89	0.48	0.58	0.61	0.44	0.58
Tl	1.36	1.33	1.15	1.17	1.16	1.19	1.22	1.29	1.24	1.69	0.46	1.33	1.41	1.20	1.28
Pb	20.35	39.85	21.77	24.87	18.98	20.44	22.93	57.18	34.40	17.43	16.30	67.28	47.00	39.60	46.03
Bi	0.02	0.17	0.03	0.02	0.06	0.02	0.02	0.44	0.42	2.16	0.06	0.07	1.36	0.19	0.21
Th	13.68	25.61	21.43	44.54	15.32	17.85	12.33	19.63	17.50	4.23	10.89	12.86	10.92	16.96	16.97
U	3.00	16.44	1.80	2.89	7.33	1.46	1.98	5.58	9.05	6.75	2.26	10.00	15.11	11.53	14.84
Sr/Y	51.90	87.32	36.56	24.36	34.64	39.32	30.56	223	57.56	3.30	108	82.92	74.23	88.90	79.55
La/Yb	180	59.12	137	362	106	108	94.42	117	58.98	8.26	81.13	47.51	65.78	69.66	60.06
ΣREE	389	188	176	482	164	151	153	220	403	35.92	261	122	207	178	220
Eu*/Eu	0.61	0.84	0.62	0.33	0.71	0.68	0.69	0.92	0.81	0.14	0.92	0.97	0.84	0.83	0.85
$(La/Yb)_N$	121	39.90	92.50	244.00	71.90	72.80	63.80	79.00	39.90	5.58	54.80	32.10	44.50	47.10	40.60

Rock type	KRGs												
	Two-mica granite			Pyroxene granite		Hornblende granite	Meta-granite-Granitic gneiss		Granodiorite				
Locality	Chaqpaala			Bongo		Bongo	Funbisi	Tongo	Funbisi		Naga	Tongo	
Sample ID	ZK03	ZK04	ZK06	BS01A	BS04	BM01	RA08	TG01C	RA03B	RA03C	NB01B	TG01D	

(*continued on next page*)

Table 4 (*continued*)

Rock type	KRGs											
	Two-mica granite			Pyroxene granite		Hornblende granite	Meta-granite-Granitic gneiss		Granodiorite			
Locality	Chaqpaala			Bongo		Bongo	Funbisi	Tongo	Funbisi		Naga	Tongo
Sample ID	ZK03	ZK04	ZK06	BS01A	BS04	BM01	RA08	TG01C	RA03B	RA03C	NB01B	TG01D
wt.%												
SiO_2	71.51	73.01	72.43	63.21	64.35	63.92	73.88	69.19	74.21	74.40	72.94	69.55
TiO_2	0.42	0.31	0.30	0.73	0.91	0.92	0.27	0.51	0.23	0.22	0.15	0.49
Al2O3	13.93	13.32	13.63	12.96	13.42	14.05	13.55	14.48	13.83	13.35	13.67	14.33
Fe_2O_{3T}	2.76	2.55	2.31	5.76	5.04	4.88	2.13	3.08	1.83	1.86	1.44	3.22
MnO	0.07	0.07	0.07	0.10	0.09	0.09	0.05	0.07	0.05	0.05	0.06	0.07
MgO	0.99	0.84	0.70	2.57	1.79	1.93	0.44	1.08	0.36	0.36	0.42	1.06
CaO	1.77	1.44	1.45	4.11	3.45	3.24	1.09	2.15	1.14	1.07	1.13	2.04
Na_2O	3.76	3.67	3.75	3.69	3.70	4.11	3.29	4.19	3.53	3.39	4.31	3.98
K_2O	4.35	4.17	4.44	4.78	4.91	4.72	5.03	4.19	4.87	4.71	4.29	4.53
P_2O5	0.20	0.15	0.13	0.74	0.51	0.49	0.08	0.23	0.07	0.07	0.08	0.26
LOI (%)	0.46	0.42	0.34	0.48	0.56	0.36	0.16	0.60	0.36	0.20	0.68	0.48
TOTAL	100.22	99.95	99.55	99.13	98.73	98.71	99.97	99.77	100.48	99.68	99.17	100.01
K_2O/Na_2O	1.16	1.14	1.18	1.30	1.33	1.15	1.53	1.00	1.38	1.39	1.00	1.14
$K_2O + Na_2O$	8.11	7.84	8.19	8.47	8.61	8.83	8.32	8.38	8.40	8.10	8.60	8.51
Mg#	41.45	39.49	37.51	46.92	41.30	43.93	29.04	40.99	28.04	27.72	36.62	39.47
A/CNK	0.99	1.01	1.00	0.69	0.76	0.79	1.06	0.94	1.05	1.06	0.99	0.95
A/NK	1.28	1.26	1.24	1.15	1.18	1.18	1.25	1.27	1.25	1.25	1.16	1.25
ppm												
Sc	5.03	4.38	3.95	10.69	8.34	10.30	3.05	4.68	2.90	3.08	2.63	4.56
V	37.39	31.51	29.24	80.70	73.01	74.68	18.66	37.92	16.42	16.52	17.63	39.10
Cr	44.64	48.30	61.47	77.35	51.14	48.44	36.91	40.94	37.94	39.38	30.91	29.66
Co	5.06	4.36	3.97	13.75	10.49	10.87	2.68	5.73	2.34	2.45	1.93	5.69
Ni	34.87	23.45	21.32	47.50	37.39	37.59	13.93	15.52	80.65	52.86	22.01	23.45
Cu	12.16	6.97	6.23	42.15	33.57	31.83	7.47	12.73	34.33	24.18	10.24	12.41
Zn	59.40	50.79	41.21	95.44	97.60	98.42	47.99	69.64	49.60	48.07	36.37	60.79
Ga	20.67	20.03	19.95	20.30	22.21	22.66	21.08	22.57	21.39	22.41	25.09	19.69
Rb	169	173	160	169	166	149	222	133	207	242	183	132
Sr	446	316	304	1275	1274	1359	168	719	164	150	387	689
Zr	206	148	168	482	640	483	168	179	135	153	130	201
Nb	13.05	12.06	12.01	9.02	14.47	14.98	10.53	6.90	8.88	10.29	8.55	7.38
Cs	4.76	4.58	3.24	6.71	6.88	4.03	6.77	10.95	4.30	6.46	4.44	11.30
Ba	1143	625	684	2020	1923	2075	948	1165	830	812	766	1191
La	62.18	29.34	35.00	91.07	135	153	56.11	41.13	58.73	76.49	19.55	43.95
Ce	118	59.06	71.04	150	268	303	98.97	87.14	99.67	137	36.83	89.59
Pr	13.68	7.25	8.63	16.32	30.43	33.64	10.52	10.52	10.78	14.46	4.94	10.71
Nd	47.17	25.34	31.64	57.19	111	122	33.90	35.47	34.18	47.39	17.87	36.56
Sm	7.81	4.17	4.83	9.98	19.53	21.68	4.43	5.62	4.44	6.96	3.22	5.83
Eu	1.61	0.97	1.06	2.49	4.16	4.69	0.72	1.32	0.64	0.69	0.81	1.41
Gd	5.66	2.95	3.39	7.09	12.91	14.59	2.89	3.88	2.99	4.89	2.15	4.16
Tb	0.68	0.36	0.41	0.78	1.43	1.60	0.31	0.41	0.31	0.54	0.26	0.44
Dy	2.95	1.58	1.83	3.30	5.92	6.56	1.18	1.69	1.13	2.04	1.16	1.87
Ho	0.52	0.29	0.34	0.57	1.00	1.09	0.20	0.27	0.18	0.32	0.20	0.30
Er	1.30	0.81	0.91	1.42	2.35	2.60	0.53	0.71	0.44	0.74	0.56	0.78
Tm	0.18	0.13	0.14	0.21	0.33	0.34	0.08	0.10	0.06	0.10	0.09	0.11
Yb	1.17	0.90	0.98	1.34	2.07	2.02	0.48	0.61	0.38	0.59	0.66	0.66
Lu	0.17	0.15	0.16	0.22	0.32	0.29	0.07	0.10	0.06	0.08	0.12	0.10
Y	15.02	9.29	10.29	16.46	26.76	32.25	6.00	8.09	5.18	9.29	6.79	8.89
Hf	6.18	5.00	5.60	13.28	17.28	13.15	5.61	5.97	4.77	5.19	7.28	6.78
Ta	1.03	0.97	1.03	0.55	1.20	1.24	1.14	0.51	0.85	1.35	0.72	0.56
Tl	0.91	0.96	0.90	1.10	1.15	0.93	1.30	1.22	1.19	1.37	1.48	1.27
Pb	19.24	21.08	22.26	35.56	37.51	30.56	20.26	43.32	21.87	23.01	81.52	43.41
Bi	0.02	0.07	0.03	0.65	0.44	0.36	0.12	2.99	0.03	0.02	0.10	0.15
Th	16.12	18.67	19.22	38.12	26.51	24.99	18.72	20.03	30.65	32.88	19.50	12.38
U	4.97	9.83	7.74	6.61	8.26	9.83	1.95	12.67	2.06	10.71	18.36	11.34
Sr/Y	29.70	33.97	29.52	77.46	47.60	42.14	28.05	88.97	31.62	16.16	56.99	77.52
La/Yb	53.19	32.45	35.86	67.86	65.38	75.80	116.41	67.10	153	131	29.57	66.19
ΣREE	278	143	171	359	621	700	216	197	219	301	95.21	205
Eu*/Eu	0.74	0.85	0.80	0.95	0.80	0.81	0.62	0.87	0.53	0.36	0.94	0.88
$(La/Yb)_N$	35.90	21.90	24.20	45.90	44.20	51.20	78.60	45.30	103.00	88.40	20.00	44.70

Rock type	KRGs											
	Granodiorite		Adamellite					Granodiorite				
Locality	Chaqpaala		Bongo		Chaqpaala			Bongo			Du-Motigu	Tongo
Sample ID	ZK01	ZK07	BS02	BS03	ZK02	ZK05	ZK08	BN03A	BN03B	BN03C	DM03B	TG01E
wt.%												
SiO_2	71.32	71.14	61.78	61.82	71.51	71.36	70.87	69.57	65.80	68.46	67.73	69.88
TiO_2	0.37	0.37	1.07	1.08	0.40	0.42	0.37	0.65	0.74	0.67	0.67	0.47

(*continued on next page*)

Table 4 (*continued*)

Rock type	KRGs											
	Granodiorite		Adamellite					Granodiorite				
Locality	Chaqpaala		Bongo		Chaqpaala			Bongo			Du-Motigu	Tongo
Sample ID	ZK01	ZK07	BS02	BS03	ZK02	ZK05	ZK08	BN03A	BN03B	BN03C	DM03B	TG01E
Al2O3	13.76	14.00	13.60	13.24	13.96	13.81	13.46	13.57	15.47	14.59	15.52	14.34
Fe_2O_{3T}	2.59	2.63	5.50	5.97	2.66	2.76	2.67	3.31	3.24	3.07	3.11	3.02
MnO	0.07	0.07	0.10	0.11	0.07	0.07	0.07	0.06	0.05	0.06	0.06	0.07
MgO	0.88	0.87	2.16	2.24	0.92	0.97	0.93	1.05	1.07	1.01	1.13	0.98
CaO	1.72	1.89	3.66	3.93	1.83	1.72	1.49	2.24	2.46	2.33	2.83	2.12
Na_2O	3.80	3.77	3.73	3.77	3.83	3.78	3.66	3.82	4.66	4.39	4.88	4.21
K_2O	4.29	4.38	4.55	4.61	4.28	4.17	4.21	3.68	3.75	3.54	3.11	3.86
P_2O5	0.19	0.18	0.55	0.62	0.20	0.21	0.19	0.23	0.23	0.21	0.32	0.19
LOI (%)	0.58	0.78	1.06	0.48	0.50	0.44	0.54	0.66	0.66	0.38	0.40	0.38
TOTAL	99.57	100.08	97.76	97.87	100.16	99.71	98.46	98.84	98.13	98.71	99.76	99.52
K_2O/Na_2O	1.13	1.16	1.22	1.22	1.12	1.10	1.15	0.96	0.80	0.81	0.64	0.92
$K_2O + Na_2O$	8.09	8.15	8.28	8.38	8.11	7.95	7.87	7.50	8.41	7.93	7.99	8.07
Mg#	40.23	39.59	43.76	42.64	40.66	41.05	40.83	38.59	39.55	39.46	41.85	39.13
A/CNK	0.98	0.97	0.77	0.72	0.98	1.00	1.01	0.95	0.96	0.95	0.94	0.96
A/NK	1.26	1.28	1.23	1.18	1.28	1.29	1.27	1.32	1.32	1.32	1.36	1.29
ppm												
Sc	4.58	4.71	9.15	11.16	5.51	4.92	4.75	4.11	4.13	4.05	4.46	4.86
V	35.82	35.83	71.99	86.90	37.73	37.68	33.89	43.94	45.09	42.02	53.47	39.97
Cr	52.10	50.99	53.17	59.28	46.00	35.88	45.22	48.30	24.41	40.13	36.66	31.17
Co	5.01	5.20	12.65	13.61	4.74	4.91	4.94	6.35	6.62	6.02	6.89	4.75
Ni	35.81	23.77	32.20	50.06	29.95	16.66	32.74	47.52	16.11	24.89	70.96	14.29
Cu	16.12	27.49	24.37	37.43	10.83	8.94	11.18	38.79	15.03	15.91	39.41	21.84
Zn	54.30	51.41	110	111	56.75	58.20	58.25	74.83	80.82	75.79	67.11	55.46
Ga	20.85	21.06	22.82	23.18	22.61	20.74	20.87	20.95	23.06	21.93	22.58	20.77
Rb	139	168	135	167	162	157	212	89.15	84.55	94.93	53.68	115
Sr	393	424	1443	1422	416	460	363	978	1245	1140	1033	672
Zr	204	197.20	546	669	216.58	232.85	235.01	249	265	270	219	151.00
Nb	12.27	11.57	15.43	15.63	15.27	13.76	12.75	6.78	5.99	5.50	7.71	6.17
Cs	3.46	5.32	2.20	7.24	4.80	3.86	8.35	6.45	7.76	6.77	2.86	12.17
Ba	993	1016	1969	2123	970	1106	854	2008	2227	2099	1084	1143
La	36.13	43.79	167	175	50.80	51.63	37.93	77.05	76.95	63.54	47.43	32.19
Ce	71.55	85.93	316	333	104	102	71.44	158	148	129	98.46	69.22
Pr	8.75	10.01	34.57	40.05	11.97	12.24	8.76	18.67	18.28	15.30	12.26	8.85
Nd	30.69	34.79	128	148	40.36	46.26	30.87	64.67	64.29	52.57	44.30	31.18
Sm	5.41	5.51	22.42	26.43	6.29	7.53	5.66	9.25	10.00	7.98	7.57	5.40
Eu	1.25	1.16	4.73	5.54	1.47	1.56	1.24	1.95	2.18	1.75	1.90	1.19
Gd	3.66	3.92	15.09	17.53	4.47	5.39	3.93	5.80	6.11	4.63	4.90	3.48
Tb	0.44	0.46	1.66	1.95	0.52	0.66	0.47	0.57	0.59	0.45	0.52	0.39
Dy	1.89	1.94	6.91	8.14	2.23	2.91	2.06	2.17	2.19	1.59	1.99	1.66
Ho	0.34	0.35	1.16	1.36	0.40	0.51	0.38	0.36	0.35	0.24	0.33	0.26
Er	0.92	0.93	2.75	3.13	1.08	1.29	1.02	0.93	0.81	0.60	0.77	0.66
Tm	0.14	0.14	0.36	0.43	0.16	0.18	0.15	0.13	0.11	0.09	0.10	0.09
Yb	0.92	0.90	2.22	2.63	1.07	1.17	1.02	0.81	0.63	0.54	0.60	0.60
Lu	0.15	0.14	0.32	0.39	0.17	0.17	0.17	0.12	0.09	0.08	0.08	0.09
Y	10.29	10.30	32.55	36.58	12.20	14.51	11.41	10.58	10.79	6.58	8.89	7.63
Hf	6.07	5.96	14.95	18.11	6.69	6.77	7.02	6.59	6.88	7.16	6.10	4.98
Ta	0.95	1.01	1.25	1.25	1.14	1.15	1.00	0.57	0.42	0.41	0.48	0.46
Tl	0.92	0.98	0.98	1.07	0.91	0.89	1.15	0.67	0.74	0.73	0.42	0.96
Pb	22.16	20.83	26.33	37.42	20.81	21.20	22.72	29.23	29.93	56.07	13.33	38.18
Bi	0.10	0.11	0.43	0.63	0.08	0.05	0.18	0.20	0.09	0.08	0.08	0.14
Th	16.09	16.87	28.34	24.19	20.86	13.57	14.46	12.70	8.97	8.94	9.39	10.43
U	5.36	7.11	7.08	8.54	11.69	4.88	6.46	8.28	4.37	5.30	3.24	9.91
Sr/Y	38.21	41.19	44.34	38.87	34.06	31.69	31.81	92.38	115	173	116	88.18
La/Yb	39.44	48.55	75.05	66.41	47.57	44.12	37.26	95.00	123	117	79.45	54.10
ΣREE	173	200	735	800	237	248	177	351	341	285	230	163
Eu*/Eu	0.86	0.76	0.77	0.79	0.85	0.75	0.80	0.81	0.85	0.88	0.95	0.84
$(La/Yb)_N$	26.70	32.80	50.10	44.90	32.10	29.80	25.20	64.20	82.80	79.20	53.70	36.60

Rock type	TTG				Pegmatite-Aplite	
	Trondhjemite				Pegmatite	Aplite
Locality	Funbisi		Du-Motigu		Funbisi	Funbisi
Sample ID	RA02A	RA02B	DM04	DM04C	RA09B	RA09A
wt.%						
SiO_2	75.68	73.33	65.57	69.18	76.16	81.89
TiO_2	0.33	0.32	0.71	0.48	0.08	0.05
Al2O3	12.72	12.88	15.41	15.00	14.19	10.94
Fe_2O_{3T}	2.86	3.49	4.13	3.20	1.32	1.15
MnO	0.07	0.07	0.10	0.13	0.04	0.05

(*continued on next page*)

Table 4 (*continued*)

Rock type	TTG				Pegmatite-Aplite	
	Trondhjemite				Pegmatite	Aplite
Locality	Funbisi		Du-Motigu		Funbisi	Funbisi
Sample ID	RA02A	RA02B	DM04	DM04C	RA09B	RA09A
MgO	0.71	0.70	1.80	1.17	0.16	0.15
CaO	2.11	2.16	2.63	2.02	0.77	0.44
Na_2O	3.90	3.99	5.04	5.07	4.46	3.04
K_2O	1.31	1.92	2.71	2.80	2.26	1.77
P_2O5	0.11	0.11	0.35	0.25	0.03	0.02
LOI (%)	0.46	0.20	0.42	0.26	0.78	0.92
TOTAL	100.26	99.17	98.87	99.56	100.25	100.42
K_2O/Na_2O	0.34	0.48	0.54	0.55	0.51	0.58
$K_2O + Na_2O$	5.21	5.91	7.75	7.87	6.72	4.81
Mg#	32.97	28.44	46.33	42.01	19.36	20.53
A/CNK	1.09	1.02	0.96	1.00	1.27	1.42
A/NK	1.62	1.49	1.37	1.32	1.45	1.58
ppm						
Sc	4.27	4.29	7.36	4.50	12.23	9.54
V	44.53	53.09	71.41	44.82	9.32	6.30
Cr	65.06	70.44	36.30	35.75	23.74	27.41
Co	6.45	6.81	10.04	6.89	0.66	0.75
Ni	26.57	32.17	21.49	16.95	11.54	10.62
Cu	12.71	16.22	26.64	8.08	6.86	4.94
Zn	45.97	41.62	125	97.82	30.83	28.98
Ga	17.07	16.95	24.82	24.99	35.66	32.96
Rb	90.66	75.34	273	283	186	168
Sr	629	714	906	614	37.50	20.81
Zr	104	173	227	151	19.07	15.99
Nb	6.22	5.51	11.79	13.04	25.36	26.77
Cs	8.18	6.65	21.60	25.62	8.70	6.21
Ba	580	667	1021	826	51.42	36.79
La	34.77	31.48	65.55	32.80	3.69	2.39
Ce	67.05	61.34	119	63.50	4.85	4.63
Pr	8.02	7.33	15.89	7.64	0.73	0.56
Nd	26.81	25.34	54.75	27.98	3.01	2.67
Sm	4.06	3.72	9.35	4.61	0.94	0.97
Eu	0.91	0.98	2.07	0.96	0.15	0.07
Gd	2.77	2.38	5.86	3.29	1.43	1.51
Tb	0.33	0.27	0.63	0.44	0.30	0.38
Dy	1.57	1.06	2.43	1.97	1.93	2.48
Ho	0.27	0.18	0.41	0.35	0.42	0.50
Er	0.73	0.49	0.93	0.83	1.22	1.45
Tm	0.10	0.07	0.12	0.11	0.20	0.24
Yb	0.68	0.49	0.71	0.69	1.38	1.77
Lu	0.11	0.08	0.10	0.10	0.21	0.28
Y	7.69	5.09	12.10	10.85	14.47	16.43
Hf	2.89	4.86	6.04	4.24	0.76	0.71
Ta	0.40	0.48	1.22	1.15	1.70	1.86
Tl	0.56	0.50	1.79	2.03	0.80	0.67
Pb	13.61	14.97	13.00	11.98	12.90	7.43
Bi	0.02	0.08	0.14	0.61	0.03	0.02
Th	9.10	5.97	13.98	7.84	3.99	4.46
U	13.42	2.44	6.79	4.19	3.04	1.39
Sr/Y	81.84	140	74.95	56.57	2.59	1.27
La/Yb	51.05	64.63	92.46	47.74	2.69	1.35
ΣREE	156	140	290	156	34.91	36.32
Eu*/Eu	0.83	1.01	0.85	0.75	0.40	0.18
$(La/Yb)_N$	34.50	43.70	62.50	32.30	1.82	0.91

the KRGs and TTGs. Biotites, together with hornblendes, usually crystallize at greater pressures in the presence of some mineralizing agents such as hydrogen and fluorine, either in greater or lesser amounts (Lalonde, 1993). Biotite data from these two rock types show a linear trend towards siderophyllite (Fe-biotite), indicating crystallization under high oxygen fugacity conditions (Esfahani et al., 2017). The solubility of Ti in biotite is highly caused by temperature. Therefore, the higher the temperature, the more soluble Ti is (Patino Douce, 1993; Esfahani et al., 2017). Some of the TiO_2 concentrations in the KRGs and TTGs are as high as 5.61 and 2.85 wt% respectively (Table 4), indicating that temperature conditions were relatively high (Esfahani et al., 2017). From the plot of Ti against Mg/Mg + Fe^{2+} (Helmy et al., 2004; Fig. 12a), the overall formation temperatures of the KRGs and TTGs were in the range of 680–720 °C, with the exception of one sample that recorded a temperature of about 740 °C.

Euhedral hornblende grains embedded in interstitial quartz and K-feldspar suggest continuous crystallization of quartz and K-feldspar after hornblende had crystallized (Mazhari et al., 2008). However, the unique suites of minerals that are produced in each granitoid rock is a function of the bulk composition of the magma, the degree of aluminum oversaturation, temperature, pressure, $a(H_2O)$, f(HF), MgO + FeO, and concentrations of certain trace elements such as B, Be, Cs, F (Clarke, 1981). The amphibole group of minerals (e.g. hornblende in this study) is suitable for geobarometry and geothermometry in calc-alkaline

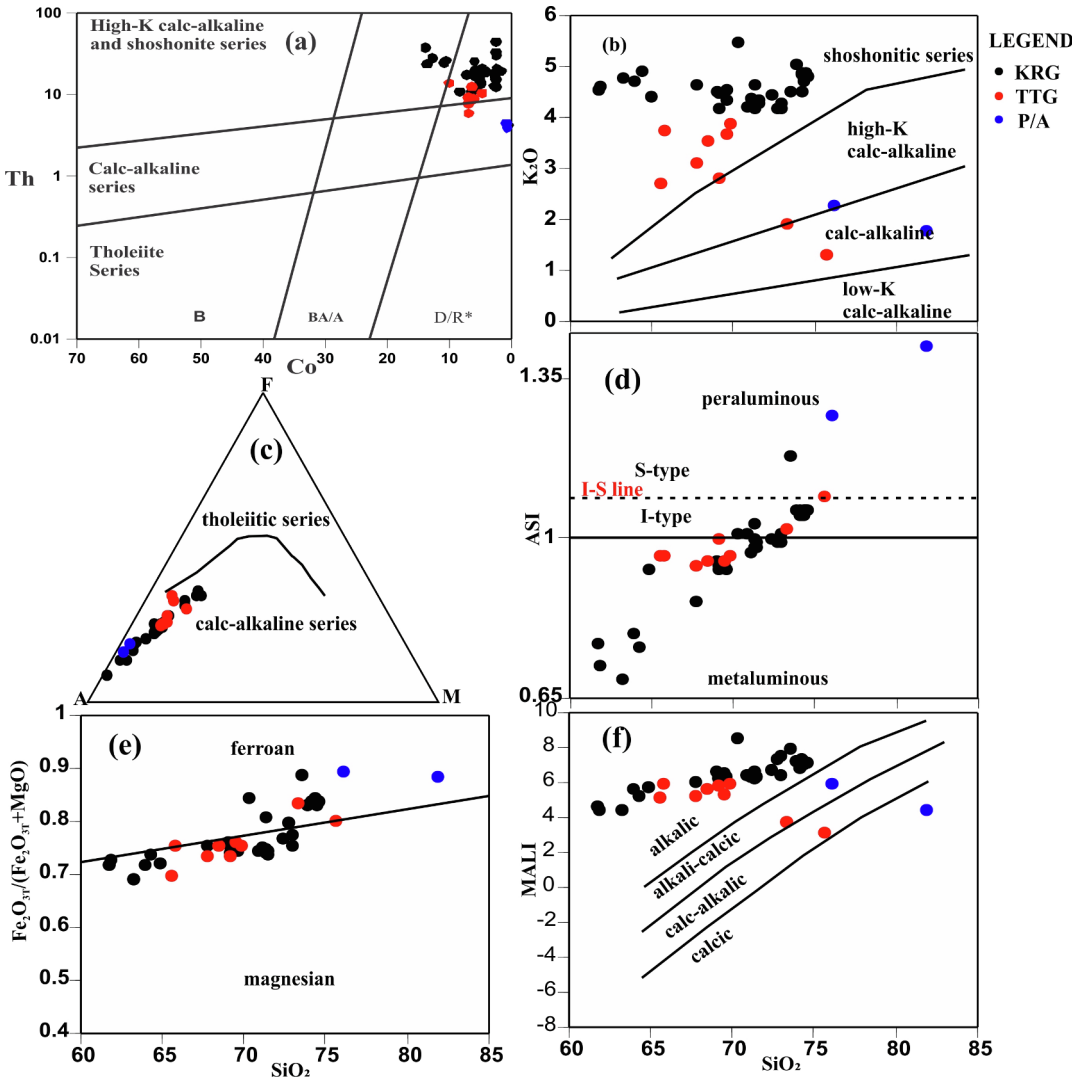

Fig. 8. (a) Th-Co diagram of Hastie et al. (2007) showing calc-alkaline to high-K calc-alkaline and shoshonitic series for the studied rocks. (b) K_2O vs. SiO_2 diagram (after Peccerillo and Taylor, 1976). (c) AFM (A = Na_2O + K_2O, F = Fe_2O_{3T}, M = MgO) diagram (after Irving and Baragar (1971)). (d) ASI vs. SiO_2 diagram (after Maniar and Piccoli, 1989). (e) Fe index, Fe_2O_{3T}/Fe_2O_{3T} + MgO vs. SiO_2 diagram (after Frost et al., 2001). (f) MALI (modified alkali lime index = Na_2O + K_2O – CaO) vs. SiO_2 diagram (after Frost et al., 2001).

igneous rocks because they are stable over a wide P-T range of 1 kbar-23 kbar and 400 °C-1150 °C (Hollister et al., 1987). Constraining the emplacement depth of granitic plutons often requires an Al-in-hornblende barometer. However, prior to that, temperature and/or oxygen fugacity parameters must be evaluated since Al content in amphibole is sensitive to crystallization conditions and oxygen fugacity (Esfahani et al., 2017). Hornblende grains from only the KRGs were analyzed in this study and they recorded temperatures of ~ 640–750 °C and pressures of ~ 2.7–4 kbar (Table 6). However, a plot of Fe^{2+}/Fe^{2+} + Mg vs. Al_{total}, reveals pressures of ~ 2–3 kbar and 6 kbar (Fig. 12b), whereas the KRGs also plot in the high fugacity field of the Fe^{2+}/Fe^{2+} + Mg vs. Al^{IV} diagram (Fig. 12c).

5.3. Petrogenesis

5.3.1. Petrogenesis of the TTGs

TTGs are known to be very important rocks in the evolution of the continental crust, and they precede the generation of KRGs (Sylvester, 1994; Manya et al., 2007; Manya, 2016). They are characterized by high concentrations of Al_2O_3 (1.08–16.5 wt%), low concentrations of HREE (Y = 3–7 ppm; Yb = 0.3–0.5 ppm), and high Sr/Y and La/Yb values (Martin, 1999; Martin et al., 2005; Manya, 2016). The TTGs of this study have similar geochemical characteristics (Table 4). They all display LREE enrichment and plot in the adakite field of the $(La/Yb)_N$ vs. Yb_N diagram (Fig. 13a), and therefore, may be classified as high silica adakites since their SiO_2 contents are greater than 60 wt%. They also display weak negative to no Eu anomalies (Fig. 10a), enrichment in Ba, Rb and Th, and negative Nb-Ta, Zr-Hf and Ti anomalies (Fig. 10b and 10c). The TTGs are co-magmatic with the fractionation of hornblende, biotite, K-feldspar, pyroxene, titanite and titanomagnetite, and to some extent plagioclase (Fig. 9). Garnet and/or amphibole may have been residual minerals in the source of the melt. The ε_{Nd}(2.1 Ga) values (+0.90 and + 1.24) of the TTGs indicate their derivation from juvenile sources (Chen and Arakawa, 2005; Sakyi et al., 2017). Similarly, the single stage Nd model ages (T_{DM1}) of 2.34–2.38 Ga and two stage Nd model ages (T_{DM2}) of 2.21–2.24 Ga (Table 5) for the TTGs further indicate their juvenile character. Therefore, the ε_{Nd} values and model ages suggest a depleted source that probably became metasomatized later in an arc system, further indicating that they were most likely produced in an almost entirely oceanic environment (e.g. Eglinger et al., 2017).

According to Drummond and Defant (1990), TTGs and adakites are formed by partial melting of hydrous basaltic crust in subduction-related settings. They may also be formed by partial melting of

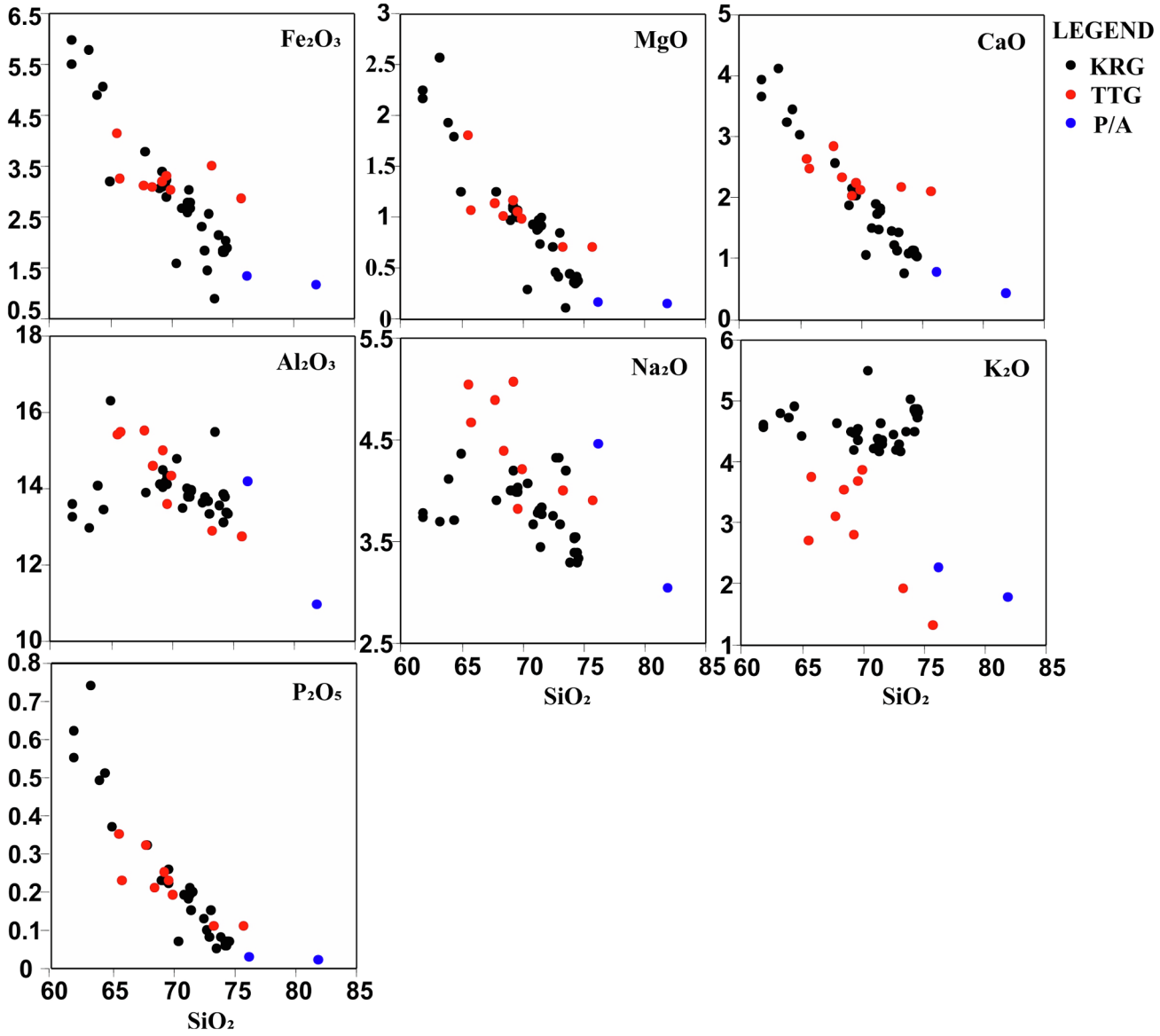

Fig. 9. Variation in major elements with SiO_2 of the KRGs, TTGs and pegmatite-aplite association showing a positive linear correlation for most of the oxides.

amphibolite/eclogite at the base of thickened arc crust (Manya, 2016). The TTGs in this study could be interpreted as adakitic arc rocks (e.g. Abitty et al., 2016) (Fig. 13a) and they show affinity to amphibolite fields in the $Al_2O_3/(FeO + MgO + TiO_2)$ vs. $Al_2O_3 + FeO + MgO + TiO_2$ diagram (Fig. 13b). We, therefore, infer that the TTGs were formed by partial melting of lower crustal materials.

5.3.2. Petrogenesis of the KRGs

The KRGs, on the other hand, have higher concentrations of K, Sr, Rb and Th, with relatively higher REE concentrations. Nonetheless, the KRGs and the TTGs share similar isotopic and geochemical signatures such as weak negative to no Eu anomalies (Fig. 10a) and negative Nb-Ta, Zr-Hf and Ti anomalies (Fig. 10b and 10c). The potassic nature of the KRGs is likely to have been derived from partial melting of low-K TTGs together with some *meta*-greywackes and metapelites, or from partial melting of a highly metasomatized K-rich mantle source (e.g., Watkins et al., 2007; Laurent et al., 2014; Eglinger et al., 2017). The presence of both positive and negative $\varepsilon_{Nd}(2.1\,Ga)$ values (-0.86 – $+1.37$) as well as Nd model ages (T_{DM1} = 2.36–2.53 Ga; T_{DM2} = 2.22–2.39 Ga), suggests that the KRGs were also derived from juvenile sources or from a short-lived mafic crust of low K_2O, but with some minor amount of older crustal input (Chen and Arakawa, 2005; Manya, 2016). The mafic (1.21–8.54 wt% Fe_2O_{3T} + MgO) and silica (61.78–74.55 wt% SiO_2) contents of the KRGs also confirm their derivation from low-K_2O magmas (Eglinger et al., 2017).

The occurrence of mafic enclaves in some of the KRGs may be indicative of mixing processes (Fig. 3). It can be inferred that the KRGs were derived by partial melting of the TTGs in which they intrude. We therefore propose the formation of the KRGs as follows: (i) crustal anatexis, most likely due to dehydration melting of mid-crustal mafic to intermediate *meta*-igneous rocks (e.g. Liégeois et al., 1998; Goswami and Bhattaacharyya, 2014; Wane et al., 2018; Lui et al., 2019), resulting in the formation of the TTGs of this study; (ii) the KRGs were then introduced by variable assimilation of old crustal materials (the TTGs) caused by the intra-plating of hot mantle-derived margins in an extensional active continental margin with lithospheric thinning. This may also be caused by continental collision, resulting in crustal thickening (evidenced by the total Al, Fe/(Fe + Mg) and Ti of the studied biotites) (e.g., Lalonde, 1993; Hawkesworth and Kemp, 2006; Hosseini et al., 2014; Liu et al., 2019).

Some of the KRG samples plot in A-type granite fields of Y vs. 10000*Ga/Al diagram (not shown). A-type granitoids are typical of

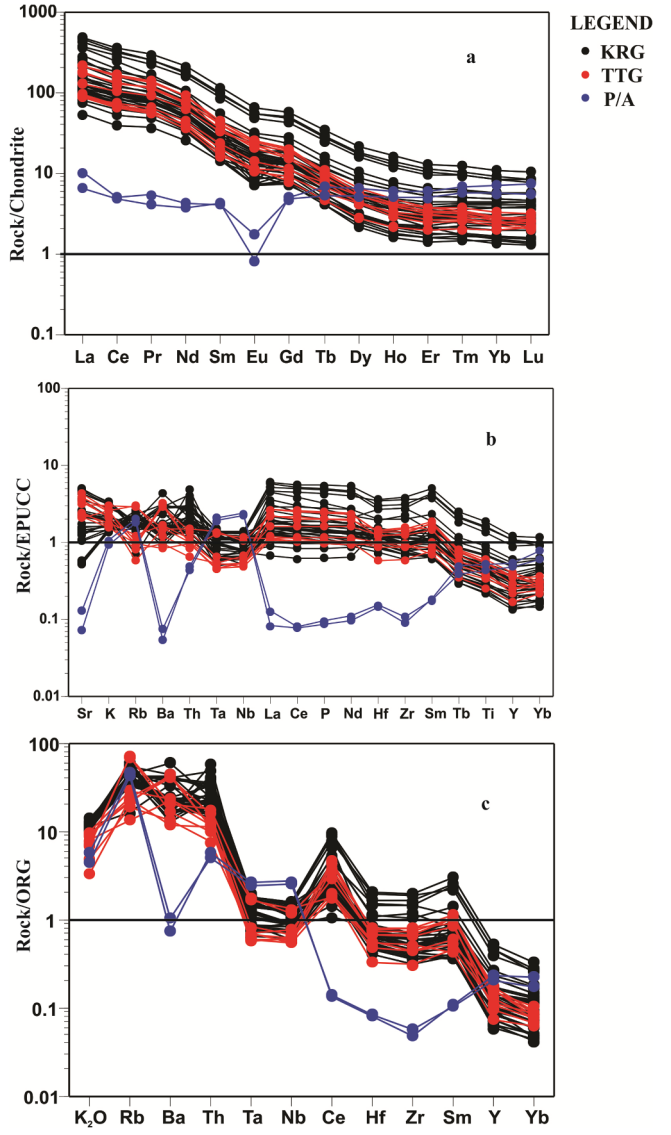

Fig. 10. (a) Chondrite-normalized spidergram (Taylor and McLennan, 1985); (b) Early Proterozoic upper continental crust-normalized multi-element diagram (Condie, 1993); and (c) Ocean ridge granite-normalized diagram (Condie, 1993) of the KRGs, TTGs and pegmatite-aplite association.

within-plate environments but rare in arcs. They are known to be anorogenic, alkaline, anhydrous and are formed when alkali basalts interact with a granulitic lower crust or by direct fractionation of the alkali basalts in stable continental blocks and rift zones without crustal interaction (e.g. Eyuboglu et al., 2019). The geochemical characteristics of the KRGs that plot in A-type granite fields are typical of I-type granitoids. We therefore speculate that the development of the A-type features was as a result of intense fractionation and does not reflect source composition or characteristics of the tectonic environment (e.g. Whalen et al., 1987; Eyuboglu et al., 2019). The Nd model ages obtained from the analyzed samples (Table 5) are slightly higher than the formation ages (2.1 Ga). The ages reflect the juvenile characteristics of the KRGs with possible minor contribution from source materials that likely contained rocks of older ages (possibly mafic lower crustal materials).

There is a clear geochemical distinction between the pegmatite-aplite association on the one hand, and the TTGs and KRGs on the other. The pegmatite and aplite are not strongly enriched in LREEs, possibly due to the presence of rutile, titanite, ilmenite and apatite as residual phases in the source of the melt (Fig. 10a). The pronounced

Table 5
Isotope data of representative KRGs and TTGs of the Bole-Nangodi Belt.

Sample ID	Rb (ppm)	Sr (ppm)	$^{87}Rb/^{86}Sr$	$^{87}Sr/^{86}Sr$	2σ err.	$(^{87}Sr/^{86}Sr)_i$	Sm (ppm)	Nd (ppm)	$^{147}Sm/^{144}Nd$	$^{143}Nd/^{144}Nd$	$(^{143}Nd/^{144}Nd)i$	2σ err.	$\varepsilon_{Nd}(t)$	TDM1 (Ga)	TDM2 (Ga)
KRGs															
BM01	148.6	1359	1.0746	0.7106	0.000014	0.6021	21.68	122.2	0.0932	0.5112	0.509911	0.000006	−0.16	2.45	2.32
BN01	173.6	1268	0.1366	0.7137	0.000020	0.6444	5.00	37.20	0.0733	0.5109	0.509886	0.000010	−0.65	2.43	2.31
RA01	213.8	361.2	1.8797	0.7548	0.000012	0.6332	7.25	61.77	0.0711	0.5109	0.509917	0.000013	−0.05	2.39	2.27
TG01G	162.0	706.5	0.2761	0.7214	0.000013	0.6298	6.11	38.52	0.0941	0.5112	0.509899	0.000007	−0.40	2.47	2.33
ZK04	173.0	315.5	1.6343	0.7475	0.000010	0.6367	4.17	25.34	0.1030	0.5113	0.509876	0.000007	−0.86	2.53	2.39
RA08	222.5	168.3	3.7532	0.8133	0.000010	0.7320	4.43	33.90	0.0792	0.5110	0.509905	0.000016	−0.28	2.42	2.30
BS02	134.6	1443	0.2791	0.7097	0.000017	0.7013	22.42	128.1	0.0948	0.5113	0.509989	0.000008	1.37	2.36	2.22
NB01B	183.1	387.2	1.8619	0.7548	0.000014	0.6458	3.22	17.87	0.0951	0.5112	0.509885	0.000014	−0.67	2.49	2.35
TTGs															
BN03B	84.55	1245	0.2569	0.7091	0.000013	0.6687	10.00	64.29	0.0808	0.5111	0.509983	0.000026	1.24	2.34	2.21
TG01E	114.6	672.4	0.5786	0.7185	0.000010	0.6491	5.40	31.18	0.0893	0.5112	0.509965	0.000006	0.90	2.38	2.24

Notes: $^{87}Rb/^{86}Sr$ and $^{147}Sm/^{144}Nd$ ratios were calculated using Rb, Sr, Sm and Nd contents, measured by ICP-MS. εNd is calculated as $[(^{143}Nd/^{144}Nd_{sample})/(^{143}Nd/^{144}Nd_{CHUR}) - 1] \times 10000$, using $(^{143}Nd/^{144}Nd)_{CHUR} = 0.512638$. Single-stage Nd model ages (TDM1) were calculated relative to the depleted mantle, and two-stage Nd model ages (TDM2) were calculated relative to the average continental crust at the time of magma crystallization (t = 2.1 Ga).

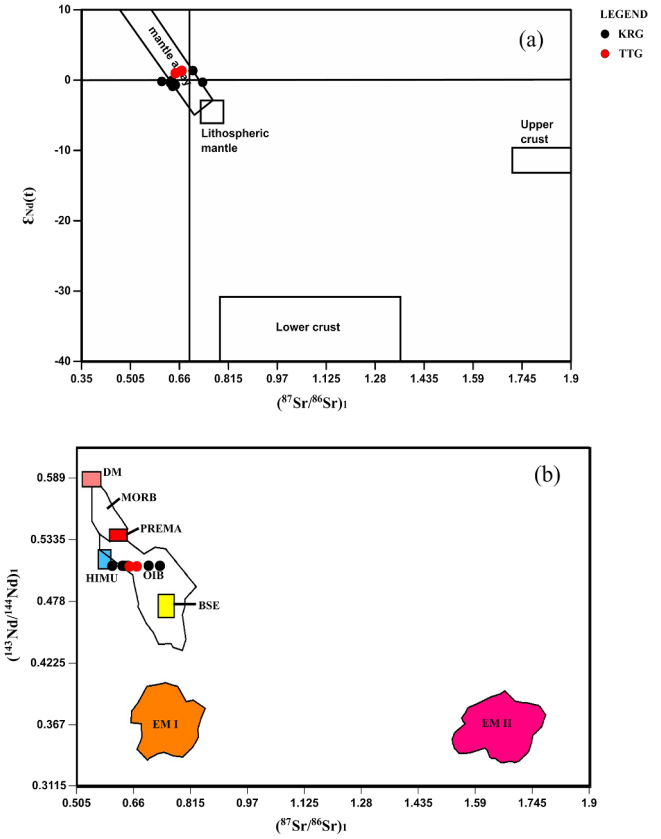

Fig. 11. (a) $\varepsilon_{Nd}(t)$ vs. $^{87}Sr/^{86}Sr_i$ diagram with mantle array and lithospheric trends after Yang et al. (2005), and lower and upper crust trend after Jahn et al. (1999). (b) $^{143}Nd/^{144}Nd$ vs. $^{87}Sr/^{86}Sr_i$ diagram with discriminant fields after Zindler and Hart (1986).

negative Eu anomalies (Fig. 10a) suggest that plagioclase may be a residual phase or was separated from the melt during fractional crystallization. They are also peraluminous, calc-alkaline and ferroan, highly evolved and plot in the metagraywacke fields of the $Al_2O_3/(FeO + MgO + TiO_2)$ vs. $Al_2O_3 + FeO + MgO + TiO_2$ diagram (Fig. 13b). However, because of their limited number in this study, no emphasis will be placed on them in our discussions on petrogenesis and tectonic setting.

5.4. Geotectonic setting

5.4.1. Tectonic setting of the TTGs and KRGs

The geochemical data of the TTGs and KRGs are enriched in LILE and LREE and depleted in HREE and HFSE. The samples display pronounced Nb-Ta and Zr-Hf troughs and weak negative or no Ti anomaly (Fig. 13). The enrichment in LILE and LREE and depletion in HREE and HFSE, coupled with the negative anomalies displayed by Nb, Ta and Ti are characteristics of subduction-related magmas and typical of rocks formed in an arc setting (e.g. Zhao and Zhou, 2007; Sakyi et al., 2014). Furthermore, the highly fractionated REEs $(La/Yb)_N$ of the granitoids, with low $(Yb)_N$ values suggest evolution of a juvenile crust (Lompo, 2009).

The calc-alkaline signatures exhibited by the granitoids suggest that they are restricted to subduction zones (Winter, 2001), and are therefore from an arc setting. In the tectonic setting discrimination diagram by Pearce et al. (1984) (Fig. 13c and 13d), the TTGs and KRGs plot mainly in the fields defined by volcanic arc granites (VAG) and Syn-COLG fields, whereas the pegmatite-aplite association plot mainly in the VAG and Syn-COLG fields (Fig. 13c) and within plate granite (WPG) field (Fig. 13d). The similarity of the tectonic settings for the granitoids,

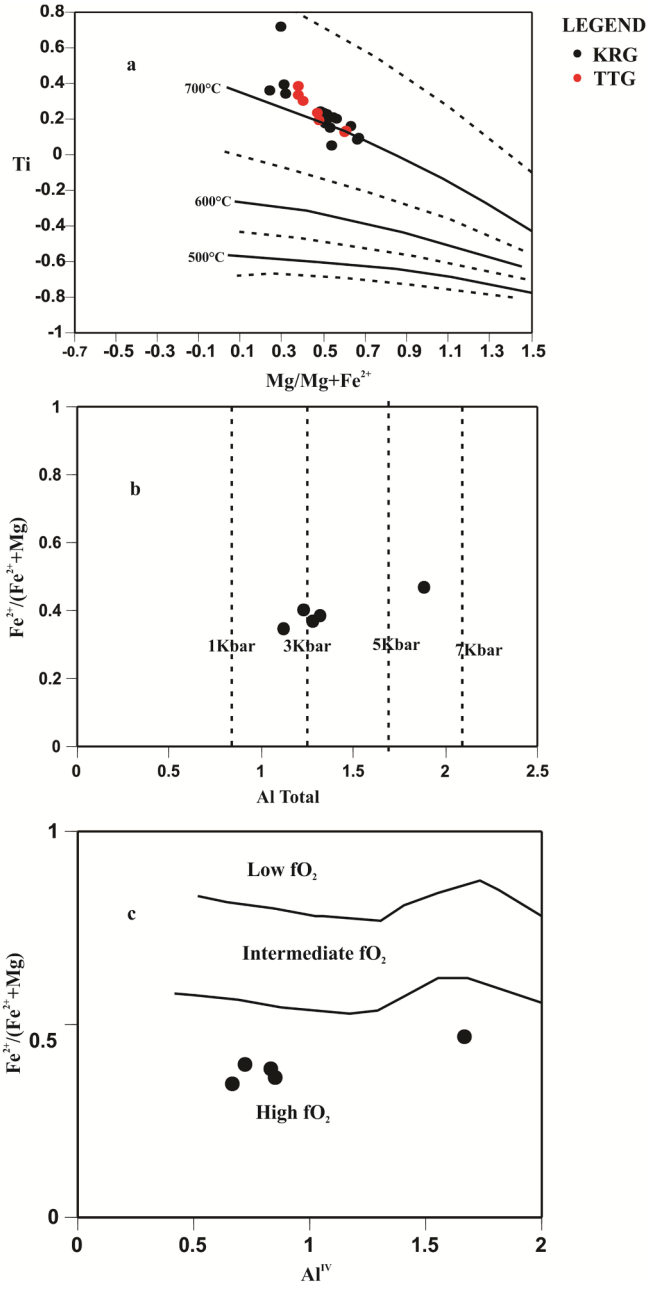

Fig. 12. (a) Ti vs. $Mg/(Mg + Fe^{2+})$ diagram (after Henry et al., 2005) on the basis of Ti-in-biotite showing formation temperatures of the TTGs and KRGs at ~ 640–750 °C. (b) $Fe^{2+}/(Fe^{2+} + Mg)$ vs Al_T diagram (Schmidt, 1992) showing formation of amphibole of the KRGs at ~ 2–6 kbar pressure. (c) $Fe^{2+}/(Fe^{2+} + Mg)$ vs Al^{IV} diagram (Anderson and Smith, 1995) showing the high fO_2 nature of amphibole of the KRGs.

derived from fluid-mobile LILE (e.g. Rb; Fig. 13c) and fluid-immobile HFSE (e.g., Nb vs. Y; 13d) strongly suggests that alteration of the rocks did not significantly affect the mobility of the LILE. The signatures further support the argument that the studied granitoids are arc rocks that formed in arc and post-collisional settings following an episode of crustal thickening.

Goswami and Bhattaacharyya (2014) and Liu et al. (2019) have explained that the melting of crustal source rocks that occurs as a result of the delamination of the lithospheric roots or slab breakoff followed by decompression generates high-K granitic magmas in *syn*-to-post collisional settings. Also, a post collisional environment marked by large movements along shear zones (evidence of shearing is observed in

Table 6
Cation and geobarometric data of representative hornblende grains from KRGs of the Bole-Nangodi Belt.

Rock type	KRGs					
Locality	Bongo					Du-Motigu
Sample ID	BN02		BS04			DM03A
Mineral	Hbl-1	Hbl-2	Hbl-1	Hbl-2	Hbl-3	Hbl-1
$(Ca + Na)_B$	1.893	1.865	1.908	1.859	1.874	2.146
Na_B	0.000	0.000	0.000	0.000	0.000	0.000
$(Na + K)_A$	0.673	0.686	0.686	0.716	0.782	0.792
$Mg/(Mg + Fe^{2+})$	0.601	0.654	0.602	0.616	0.634	0.537
$Fe^{3+}/(Fe^{3+} + Al^{VI})$	0.517	0.508	0.537	0.582	0.506	0.836
P(kbar) (Probe-Amph)						
Hammarstrom and Zen (1986)			3.1	2.7	2.5	5.6
Hollister et al. (1987)			3.1	2.7	2.4	5.9
Johnson and Rutherford (1989)			2.4	2.1	1.9	4.5
Schmidt (1992)			3.6	3.3	3.1	6

photomicrographs of KRGs) can trigger the re-melting of an earlier subduction-generated segment, either in the lithospheric mantle or lower crust, giving rise to subduction-type magmas (Liégeois et al., 1998; Wane et al., 2018). The constituent amphiboles in the KRGs are calcic, pointing to an I-type nature with emplacement in a subduction zone related to an active continental margin (e.g. Chappell et al., 2012; Sakyi et al., 2014; Esfahani et al., 2017; Eyuboglu et al., 2019; Liu et al., 2019). Typical of I-type rocks, the KRGs are interpreted to be derived from mafic igneous materials (lower crustal sources), commonly in convergent margins and collisional settings (Liu et al., 2019).

5.4.2. Regional geotectonic setting implications

The Paleoproterozoic terranes of the WAC significantly represent Archean greenstone terranes, with respect to their structural style and composition. Like the Archean, the Paleoproterozoic terranes are shrouded in controversies regarding the tectonic processes responsible for their formation. Interpretations of their tectonic setting vary between generation of the Birimian juvenile crust in arc environments or subduction-related models (e.g. Asiedu et al., 2004; Dampare et al., 2008; Mortimer, 1992; Pohl and Carlson, 1993; Sylvester and Attoh, 1992) or from plume-related magmatism (e.g. Abouchami et al., 1990). Most of these models were based on isotopic and geochemical compositions of volcanic rocks from these greenstone belts, with some contributions from the sedimentary units and the associated granitoid intrusions. These geotectonic models apply to the Paleoproterozoic Birimian rocks of Ghana and elsewhere in the WAC, as they form part of the Eburnean (2.2–2.1 Ga) orogenic event of juvenile crustal accretion, recognized in the WAC.

However, most authors who have worked on the Paleoproterozoic Birimian rocks of Ghana favour the arc setting and subduction-related models (e.g. Taylor et al., 1992; Asiedu et al., 2004; Harcouet et al., 2007; Dampare et al., 2008; de De Kock et al., 2011; Nyarko et al., 2012; Sakyi et al., 2014; Anum et al., 2015; Abitty et al., 2016; Block et al., 2016b; Petersson et al., 2016; Sakyi et al., 2017; Dampare et al., 2019; McFarlane et al., 2019). Similarly, arc tectonic settings have been proposed based on studies of granitoids that occur elsewhere in the WAC (e.g. Boher et al., 1992; Mortimer, 1992; Baratoux et al., 2011; Ganne et al., 2014; Eglinger et al., 2017; Wane et al., 2018).

For example, U-Pb zircon dating, combined with Hf-isotope geochemical data obtained from a suite of mafic and felsic potassic plutonites in Guinea suggests a juvenile crust extracted from a depleted mantle source but later metasomatized in arc systems (Eglinger et al., 2017). According to Liégeois et al. (1998) a post-collisional environment, marked by large movements along shear zones may cause the re-melting of an older continental crust generated as a result of subduction in the lithospheric mantle or the lower crust. This process leads to the generation of subduction-type melts. Furthermore, high-K calc-alkaline

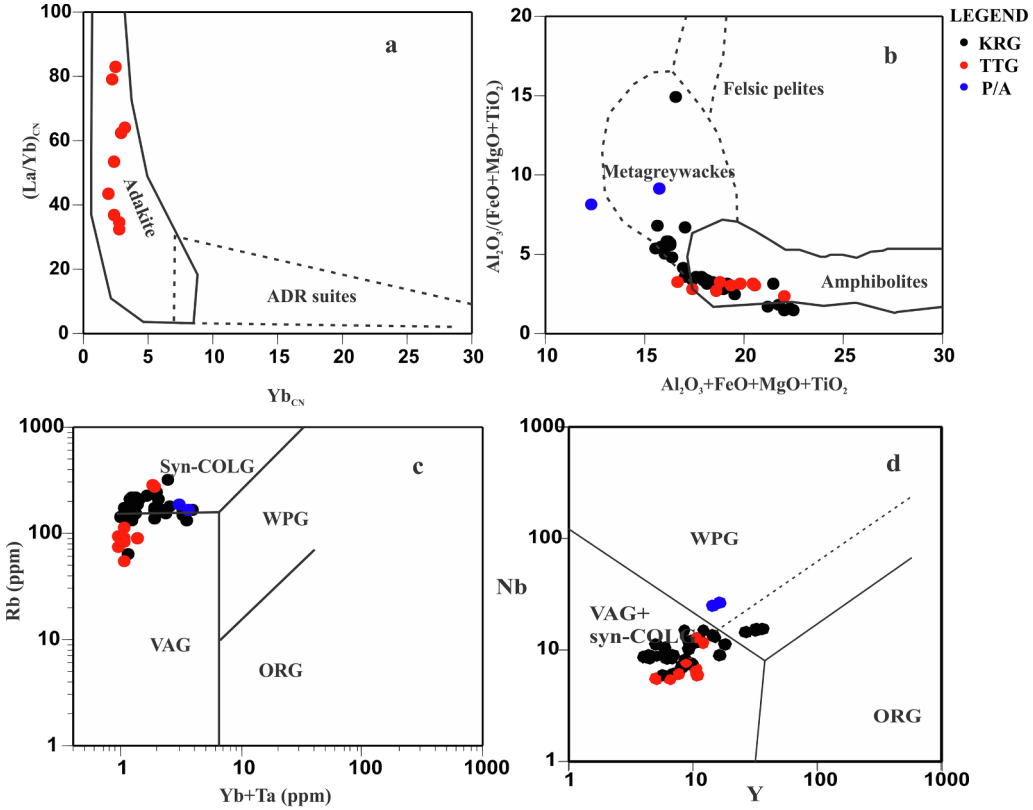

Fig. 13. (a) Chondrite normalized plot of La/Yb vs. Yb (Martin, 1986) for the TTGs, (b) $Al_2O_3/(FeO + MgO + TiO_2)$ vs. $Al_2O_3 + FeO + MgO + TiO_2$ diagram (Wolf and Wyllie, 1994), (c) Rb vs. Yb + Ta and (d) Nb vs Y tectonic discrimination diagram for granitoids (Pearce et al., 1984).

and shoshonitic granitoids are generally emplaced in arc and post collisional settings preceded by an episode of crustal thickening; a widespread feature of orogenic collisional orogens (Lu et al., 2015; Eglinger et al., 2017).

Additionally, zircon U-Pb dating and Hf and O isotope studies of igneous rocks from the Paleoproterozoic Baoulé-Mossi domain of the WAC, covering Burkina Faso, Ghana, Guinea and Mali revealed the juvenile isotopic character of the domain, and further showed that the southern part of the WAC evolved by accretionary processes (Parra-Avila et al., 2017, 2018). Similar to the above, zircon U-Pb age and Lu-Hf isotopic data from granites of southern, southeastern and northwestern Ghana suggest juvenile crustal addition with a short period of reworking of Archaean crust within the Paleoproterozoic Birimian terrane of Ghana, and further provide evidence of subduction-related crustal growth (Petersson et al., 2016, 2018). Similarly, petrographic, geochemical and geochronological studies of granitoids of the Massigui region of southern Mali, revealed that the Birimian Baoulé-Mossi segment of the WAC formed through the accretion of a complex system of oceanic island arcs (Wane et al., 2018). The authors further proposed a model summarized as follows; (1) melting of subduction-enriched mantle by oceanic plate subduction, followed by (2) an oceanic closure through oblique collision, and finally, (3) the metacratonization of the WAC, leading to the rise and emplacement of granitoid melts.

The above-mentioned tectonic settings and processes represent one of several that have been proposed for the WAC in other studies, and they are analogous to what has been proposed for the TTGs and KRGs of the Bole-Nangodi Belt of northern Ghana. Thus, the geochemical and Nd isotopic data in this study are consistent with the juvenile character of the rocks, and the island arc model, which views the Paleoproterozoic terranes of the WAC in the context of subduction-accretion processes.

Globally, the Paleoproterozoic era (c.a. 2.5–1.6 Ga) witnessed the main episode of crustal growth that was recorded on present-day continents (Giustina et al., 2009). The Paleoproterozoic was marked by a sequence of geotectonic events that led to the formation of orogenic belts and was characterized by large-scale collisional and post-collisional magmatic activity evidenced in most of the ancient cratons. Studies have shown that this global event was related to the assembly of the supercontinent Columbia (Nuna) in the Late Paleoproterozoic–Mesoproterozoic (e.g., Rogers and Santosh, 2002; Zhao et al., 2004; Meert, 2012;), particularly at about c.a. 1.90–1.85 Ga (Rogers and Santosh, 2009). Zhao et al. (2002), on the other hand, proposed that the assembly of the supercontinent Columbia (Nuna) was completed by global-scale collisional events during the Paleoproterozoic (c.a. 2.1–1.8 Ga). Rogers and Santosh (2002) proposed that between c.a. 1.9 and 1.5 Ga, South America was sutured onto West Africa whilst the eastern part of India was once connected to the western part of North America, as part of Columbia. Based on the aforementioned, we speculate that the subduction-accretion processes that prevailed in the Paleoproterozoic terrane of the WAC during the c.a. 2.1–2.0 Ga Eburnean orogeny may have played a role in the buildup of the Columbia supercontinent during the Paleoproterozoic.

6. Conclusions

The KRGs of this study consist of granite, granodiorite and adamellite, whereas the trondhjemite and granodiorite make up the TTGs. The KRGs intrude the TTGs and they are geochemically similar. The trace element and Nd-isotopes of the TTGs suggest that they were formed by partial melting of hydrous basaltic crust at pressures where garnet and amphibole were the stable phases. In this part of the Paleoproterozoic terrane of the WAC, it can be inferred that the KRGs were most likely derived from partial melting of the TTGs into which they intrude. Lastly, the pegmatite-aplite association was most likely derived at a later time, after the formation of the KRGs. To this effect, the following stages may represent the evolutionary history of the rocks that occur in the Bole-Nangodi belt of the Paleoproterozoic Birimian terrane of Ghana; (i) the generation of basaltic magmas as a result of subduction processes that led to the formation of a basaltic crust, (ii) volcanism and contemporaneous sedimentation that led to the formation of large batholiths present today as the TTGs. Hence, the formation of a juvenile arc crust (a young continental crust), known in this study as the Birimian crust, (iii) subsequent continued subduction that triggered an arc-continent collision, where the Birimian crust collided with an unknown crust, resulting in the termination of the subduction, (iv) post-collision extensional processes leading to the generation of magmas with compositions influenced by the TTGs as a result of partial melting triggered by subduction related metasomatism. These melts may have been emplaced and underplated in the lower continental crust and through the process of MASH (melting, assimilation, storage and homogenization) were transformed into more felsic melts. Subsequently, differentiation processes such as assimilation and fractional crystallization led to the generation of the KRGs. Later relaxation processes may have led to the generation of the pegmatite-aplite rock association. From the available literature and foregoing discussions, the major process operating in the Paleoproterozoic era and during the Eburnean orogeny in the WAC were subduction-accretionary processes, giving rise to the emplacement of rocks in island arc tectonic settings.

Acknowledgements

This project was made possible with financial support from the University of Ghana Research Fund (UGRF/18/1LG-044/2014-2015), Youth Innovation Promotion Association, Chinese Academy of Sciences (2016067) and the University of Ghana Earth Science Capacity Building Project. We are also very grateful to the Ghana Geological Survey Authority for helping with acquisition of maps and logistics for the field work, and processing of samples for further analysis. We also thank the technicians of the Department of Earth Science, University of Ghana who also helped in sample preparation for analysis. Nicolas Thebaud, Peter A. Cawood and an anonymous reviewer are warmly acknowledged for their careful and constructive reviews, which considerably improved this paper.

Appendix A. Supplementary data

Supplementary data to this article can be found online at https://doi.org/10.1016/j.precamres.2019.105492.

References

Abitty, E.K., Dampare, S.B., Nude, P.M., Asiedu, D.K., 2016. Geochemistry and petrogenesis of the K-rich 'Bongo-type' granitoids in the Paleoproterozoic Bole-Nangodi belt of Ghana. J. Afr. Earth Sci. 122, 47–62.

Abouchami, W., Boher, M., Michard, A., Albarède, F., 1990. A major 2.1 Ga event of mantle magmatism in West Africa: An early stage of crustal accretion. J. Geophys. Res. 95, 17605–17629.

Altherr, R., Holl, A., Hegner, E., Langer, C., Kreuzer, H., 2000. High-potassium, calc-alkaline, I-type plutonism in the European Variscides: northern Vosges (France) and northern Schwarzwald (Germany). Lithos 50, 51–73.

Amponsah, P.A., Salvi, S., Béziat, D., Baratoux, L., Siebenaller, L., Nude, P.M., Nyarko, R.S., Jessell, M.W., 2016. The Bepkong gold deposit, northwestern Ghana. Ore Geol, Rev. 78, 718–723.

Amponsah, P.A., Salvi, S., Béziat, D., Siebenaller, L., Jessell, M.W., 2015. Geology and geochemistry of the shear-hosted Julie gold deposit, NW Ghana. J. Afr. Earth Sci. 112, 505–523.

Anderson, J.L., Smith, D.R., 1995. The effects of temperature and fO_2 on the Al-in hornblende barometer. Am. Mineral. 80, 549–559.

Anum, S., Sakyi, P.A., Su, B.-X., Kwayisi, D., Dampare, S.B., Anani, C.Y., Nude, P.M., 2015. Geochemistry and geochronology of granitoids in the Kibi-Asamankese area of the Kibi-Winneba belt, southern Ghana. J. Afr. Earth Sci. 102, 166–179.

Asiedu, D.K., Dampare, S.B., Sakyi, P.A., Banoeng-Yakubo, B., Osae, S., Narko, B.J.B., Manu, J., 2004. Geochemistry of Paleoproterozoic metasedimentary rocks from the Birin diamondiferous field, southern Ghana: Implications for provenanve and crustal evolution at the Archaean-Proterozoic boundary. Geochem. Journ. 38, 215–228.

Attoh, K., 1982. Structure, Gravity models and stratigraphy of an early Proterozoic volcanic-sedimentary belt in northeastern Ghana. Precambrian Res. 18, 276–290.

Baratoux, L., Metelka, V., Naba, S., Jessel, W.M., Gregoire, M., Ganne, K., 2011. Juvenile

Paleoproterozoic crust evolution during the Eburnean orogeny (2.2-2.0 Ga), western Baukina Faso. Precambrian Res. 191, 18–45.
Block, S., Baratoux, L., Zeh, A., Laurent, O., Bruguier, O., Jessell, M., Ailleres, L., Sagna, R., Parra-Avila, L.A., Bosch, D., 2016a. Paleoproterozoic juvenile crust formation and stabilization in the south-eastern West African Craton (Ghana); New insights from U-Pb-Hf zircon data and geochemistry. Precambrian Res. 287, 1–30.
Block, S., Jessell, M., Ailleres, L., Baratoux, L., Bruguier, O., Zeh, A., Bosch, D., Caby, R., Mensah, E., 2016b. Lower crust exhumation during Paleoproterozoic (Eburnean) orogeny, NW Ghana, West African Craton: Interplay of coeval contractional deformation and extensional gravitational collapse. Precambrian Res. 274, 82–109.
Boher, M., Abouchami, W., Michard, A., Albaréde, F., Arndt, N.T., 1992. Crustal growth in West Africa at 2.1 Ga. J. Geophys. Res. 97, 345–369.
Chappell, B.W., Bryant, C.J., Wyborn, D., 2012. Peraluminous I-type granites. Lithos 153, 142–153.
Chen, B., Arakawa, Y., 2005. Elemental and Nd-Sr isotopic geochemistry of granitoids from the West Junggar fold belt (NW China), with implications for Phanerozoic continental growth. Geochim. Cosmochim. Acta 69, 1307–1320.
Christofides, G., Perugini, D., Koroneos, A., Soldatos, T., Poli, G., Eleftheriadis, G., Del Moro, A., Neiva, A.M., 2007. Interplay between geochemistry and magma dynamics during magma interaction: An example from the Sithonia Plutonic Complex (NE Greece). Lithos 95, 243–266.
Chu, Z.Y., Wu, F.Y., Walker, R.J., Rudnick, R.L., Pitcher, L., Puchtel, I.S., Yang, Y.H., Wilde, S.A., 2009. Temporal evolution of the lithospheric mantle beneath the eastern North China Craton. J. Petrol. 50, 1857–1898.
Chu, Z.Y., Yang, Y.H., Guo, J.H., Qiao, G.S., 2011. Calculation method for direct internal mass fractionation correction of spiked isotopic ratios from multi-collector mass spectrometric measurements. Int. J. Mass Spectrom. 299, 87–93.
Clarke, D.B., 1981. The mineralogy of peraluminous granites: a review. Can. Mineral. 19, 3–17.
Condie, K.C., 1993. Chemical composition and evolution of the upper continental crust: Contrasting results from surface samples and shales. Chem. Geol. 104, 1–37.
Dampare, S.B., Shibata, T., Asiedu, D.K., Okano, O., Osae, S.K.D., Atta-Peters, D., Sakyi, P.A., 2019. Ultramafic-mafic and granitoids supra-subduction magmatism in the southern Ashanti volcanic belt, Ghana: Evidence from geochemistry and Nd isotopes. Geol. J. 1–37.
Dampare, S.B., Shibata, T., Asiedu, D.K., Osae, S., Banoeng-Yakubo, B., 2008. Geochemistry of Paleoproterozoic metavolcanics rocks from the Southern Ashanti volcanic belt, Ghana: Petrogenetic and tectonic setting implications. Precambrian Res. 162, 403–423.
de De Kock, G.S., Armstrong, R.A., Siegfried, H.P., Thomas, E., 2011. Geochronology of the Birim Supergroup of the West African Craton in the Wa-Bole region of west-central Ghana: Implications for the stratigraphic framework. J. Afr. Earth Sci. 59, 1–40.
Deer, W.A., Howie, R.A., Zussman, J., 1992. An Introduction to the Rock-Forming Minerals, 2nd Ed. Longman, London, pp. 696p.
DePaolo, D. J., 1998. Nd isotope geochemistry. An introduction. Spriger, Berlin, Germany, pp. 187.
Drummond, M.S., Defant, M.J., 1990. A model for trondhjemite-tonalite-dacite genesis and crustal growth via slab melting. J. Geophys. Res. 95, 21503–21521.
Eglinger, A., Thebaud, N., Zeh, A., Davis, J., Miller, J., Parra-Avila, L.A., Loucks, R., McCuaig, C., Belousova, E., 2017. New insights into crustal growth of the Paleoproterozoic margin of the Archaean Kemena-Man domain, West African craton (Guinea): Implications of gold mineral system. Precambrian Res. 292, 258–289.
Eleftherriadis, G., Koroneos, A., 2003. Geochemistry and petrogenesis of post-collision Pangeon granitoids in Central Macedonia. Northern Greece. Chem. Erde 63, 364–389.
Esfahani, M.M., Khalili, M., Bakhshi, M., 2017. Petrogenesis of Soheyle-Pakuh and Golshekanan granitoid based on mineral chemistry of ferromagnesian minerals (north of Nain). Iran. J. Afr. Earth Sci. 129, 973–986.
Eyuboglu, Y., Dudas, F.O., Zhu, D.-Z., Liu, Z., Chatterjee, N., 2019. Late Cretaceous I- and A-type magmas in eastern Turkey: Magmatic response to double-sided subduction of Paleo- and Neo-Tethyan lithospheres. Lithos 326, 39–70.
Feybesse, J.L., Billa, M., Guerrot, C., Duguey, E., Lescuye, J.L., Jean-Pierre Milesi, J.P., Bouchot, V., 2006. The Paleoproterozoic Ghanaian province: geodynamic model and ore controls, including regional stress modeling. Precambrian Res. 149, 149–169.
Frost, B.R., Barnes, C.G., Collins, W.J., Arculus, R.J., Ellis, D.J., Frost, C.D., 2001. A Geochemical classification for granitic rocks. J. Petrol. 42, 2033–2048.
Ganne, J., Gerbault, M., Block, S., 2014. Thermo-mechanical modeling of lower crust exhumation – Constraints from the metamorphic record of the Paleoproterozoic Eburnean Orogeny, West African Craton. Precambrian Res. 243, 88–109.
Giret, A., Bonin, B., Leger, J.M., 1980. Amphibole compositional trends in oversaturated and undersaturated alkaline plutonic ring-complexes. Can. Mineral. 18, 481–495.
Giustina, M.E.S.D., de Oliveira, C.G., Pimentel, M.M., de Melo, L.V., Fuck, R.A., Dantas, E.L., Buhn, B., 2009. U-Pb and Sm-Nd constraints on the nature of the Campinorte sequence and related Palaeoproterozoic juvenile orthogneisses, Tocantins Province, central Brazil. Geol. Soc. London, Spec. Publicat. 323, 255–269.
Goswami, B., Bhattaacharyya, C., 2014. Petrogenesis of shoshonitic granitoids, eastern India: Implications for the late Grenvillian post-collisional magmatism. Geosci. Front. 5, 821–843.
Hammarstrom, J.M., Zen, E., 1986. Aluminium in hornblende: an empirical igneous geobarometer. Am. Mineral. 89, 317–329.
Harcouet, V., Guillou-Frottier, L., Bonneviel, A., Bouchot, V., Milesi, J.-P., 2007. Geological and thermal conditions before the major Paleoproterozoic gold-mineralization event at Ashanti, Ghana, as inferred from improved thermal modeling. Precambrian Res. 113, 1–8.
Hastie, A.R., Kerr, A.C., Pearce, J.A., Mitchell, S.F., 2007. Classification of altered volcanic island arc rocks using immobile elements: development of the Th-Co discrimination diagram. J. Petrol. 48, 2341–2357.
Hawkesworth, C., Kemp, A., 2006. Using hafnium and oxygen isotopes in zircons to unravel the record of crustal evolution. Chem. Geol. 226, 144–162.
Hein, K.A.A., 2010. Succession of structural events in the Goren greenstone belt (Burkina Faso): implications for West African tectonics. J. Afr. Earth Sci. 56, 83–94.
Helmy, H.M., Ahmed, A.F., El Mahallawi, M.M., Ali, S.M., 2004. Pressure, temperature and oxygen fugacity conditions of calc-alkaline granitoids, Eastern Desert of Egypt, and tectonic implications. J. Afr. Earth Sci. 38, 255–268.
Henry, D.J., Guidotti, C., Thomas, J.A., 2005. Ti-saturation surface for low-to medium pressure metapelitic biotites: implications for geothermometry and Ti-saturation mechanisms. Am. Mineral. 90, 316–328.
Hirdes, W., Davis, D.W., Eisenlohr, B.N., 1992. Reassessment of Proterozoic granitoid ages in Ghana based on U-Pb zircon and monazite dating. Precambrian Res. 56, 89–96.
Hollister, L.S., Grissom, G.C., Peters, E.K., Stowel, H.H., Sisson, V.B., 1987. Confirmation of the empirical correlation of Al in hornblende with pressure of solidification of calc-alkaline plutons. Am. Mineral. 72, 231–239.
Hosseini, E.S., Ardalan, A.A., Emami, M.H., Razavi, M.H., 2014. The petrology and geochemistry pf granitoid rocks in the Troud Area of Northeastern Shahrood. Iranian J. Earth Sci. 6, 64–77.
Huang, X.-L., Niu, Y., Xu, Y.-G., Chen, L.-L., Yang, Q.-J., 2010. Mineralogical and geochemical constraints on the petrogenesis of post-collisional potassic and ultrapotassic rocks from western Yunnan, SW China. J. Petrol. 51, 1617–1654.
Irving, T.N., Baragar, W.R.A., 1971. A guide to the chemical classification of the common volcanic rocks. Can. J. Earth Sci. 8, 523–548.
Jahn, B.-M., Wu, F.Y., Lo, C.H., Tsai, C.H., 1999. Crust-mantle interaction induced by deep subduction of the continental crust: geochemical and Sr-Nd isotopic evidence for post-collisional mafic-ultramafic intrusions of the Northern Dabie Complex, Central China. Chem. Geol. 157, 119–146.
Jin, X., Zhu, H., 2000. Determination of 43 trace elements in rock samples by double focusing high resolution inductively coupled plasma-mass spectrometer. Chinese J. Anal. Chem. 5, 563–567.
Johnson, M.C., Rutherford, M.J., 1989. Experiments calibration of the aluminum-in-hornblende geobarometer with application to Long Valley Caldera (California) volcanic rocks. Geology 17, 837–841.
Lalonde, A.E., 1993. Composition and color of biotite from granites: Two useful properties in the characterization of plutonic suites from the Hepburn zone of Wopmay Orogen, Northwest Territories. Canad. Mineral. 31, 203–217.
Laurent, O., Martin, H., Moyen, J.F., Doucelance, R., 2014. The diversity and evolution of late-Archaean granitoids: evidence for the onset of modern-style plate tectonics between 3.0 and 2.5 Ga. Lithos 205, 208–235.
Leake, B.E., Wooley, A.R., Arps, C.E.S., Birch, W.D., Gilbert, M.C., Grice, J.D., Hawthorne, F.C., Kato, A., Kisch, H.J., Krivivichev, V.G., Linthout, K., Laird, J., Mandarino, J.A., Maresch, W.V., Nickel, E.H., Rock, N.M.S., Schumacher, J.C., Smith, D.C., Stephenson, N.C.N., Ungaretti, L., Whittaker, E.J.W., Youzhi, G., 1997. Nomenclature of amphiboles: report of the subcommittee on amphiboles of the International Mineralogical Association, commission on new minerals and mineral names. Am. Mineral. 82, 1019–1037.
Leube, A., Hirdes, W., Mauer, R., Kesse, G.O., 1990. The Early Proterozoic Birimian Supergroup of Ghana and some aspects of its associated gold mineralization. Precambr. Res. 46, 139–165.
Liégeois, J.P., Navez, J., Hertogen, J., Black, R., 1998. Contrasting origin of post-collisional high-K calc-alkaline and shoshonitic versus alkaline and peralkaline granitoids. The use of sliding normalization. Lithos 45, 1–28.
Liégeois, J.P., Claessens, W., Camara, D., Klerkx, J., 1991. Short-lived Eburnian orogeny in southern Mali. Geology, tectonics, U-Pb and Rb-Sr geochronology. Precambrian Res. 50, 111–136.
Lindsley, D.H., 1983. Pyroxene thermometry. Am. Mineral. 68 (2), 477–493.
Liu, X., Liu, W., Si, C., 2019. Petrogenesis and source rocks of the high-K calc-alkaline and shoshonitic I-type granitoids in the northwestern part of East Junggar, NW China. Lithos 326–327, 298–312.
Lompo, M., 2009. Geodynamic evolution of the 2.25–2.0 Ga Paleoproterozoic magmatic rocks in the Man-Leo Shield of the West African Craton. A model of subsidence of an oceanic plateau. Geol. Soc. Lond. Spec. Publ. 323, 231–254.
Lu, Y.-J., McCuaig, T.C., Li, Z.-X., Jourdan, F., Hart, C.J.R., Hou, Z.-Q., Tang, S.-H., 2015. Paleogene post-collisional lamprophyres in western Yunnan, western Yangtze craton: ante source and tectonic implications. Lithos 233, 139–161.
Maniar, P.D., Piccoli, P.M., 1989. Tectonic discrimination of granitoids. Geol. Soc. Am. Bull. 101, 635–643.
Manya, S., 2016. Petrogenesis and emplacement of the TTG and K-rich granites at the Buzwagi gold mine, northern Tanzania: implications for the timing of gold mineralization. Lithos 256–257, 26–40.
Manya, S., Maboko, M.A.H., Nakamura, E., 2007. Geochemistry of high-Mg andesite and associated adakitic rocks in the Musoma–Mara Greenstone Belt, Northern Tanzania: possible evidence for Neoarchaean ridge subduction? Precambrian Res. 159, 241–259.
Martin, H., 1986. Effect of steeper Archaean geothermal gradient on geochemistry of subduction zone magmas. Geology 14, 753–756.
Martin, H., 1999. Adakitic magmas: modern analogue to Archaean granitoids. Lithos 46, 411–429.
Martin, H., Smithies, R.H., Rapp, R., Moyen, J.F., Champion, D., 2005. An Overview of adakite, tonalite–trondhjemite–granodiorite (TTG) and sanukitoid: relationships and some implications for crustal evolution. Lithos 79, 1–24.
Mazhari, S.A., Bea, F., Amani, S., Ghalamghash, J., 2008. Estimation of temperature and pressure of intrusive rocks crystallization: a case study of Naqadeh, Pasveh and Delkeh Plutons, W Iran. . J. Appl. Sci. 8 (6), 934–945.

McFarlane, H.B., Ailleres, L., Betts, P., Ganne, J., Baratoux, L., Jessell, M.W., Block, S., 2019. Episodic collisional orogenesis and lower crust exhumation during the Paleoproterozoic Eburnean Orogeny: evidence from the Sefwi Greenstone Belt, West African Craton. Precambrian Res. 325, 88–110.
Meert, J.G., 2012. What's in a name? The Columbia (Paleopangaea/Nuna) supercontinent. Gondwana Res. 21, 987–993.
Milési, J.P., Ledru, P., Feybesse, J.L., Dommanget, A., Marcoux, E., 1992. Early Proterozoic ore deposits and tectonics of the Birimian orogenic belt, West Africa. Precambrian Res. 58, 305–344.
Mortimer, J., 1992. Lithostratigraphy of the early Proterozoic Toumodi Volcanic Group in Central Côte d'Ivoire: Implications for Birimian stratigraphy models. J. Afr. Earth Sci. 14, 81–91.
Nesbitt, H.W., Young, G.M., 1982. Early Proterozoic climates and plate motions inferred from major element chemistry of lutites. Nature 299, 715–717.
Nyarko, E.S., Asiedu, D.K., Osae, S., Dampare, S., Hanson, J., Osei, J., Enti-Brown, S., Tulasi, D., 2012. Geochemical characteristics of the basin-type granitoids in the Winneba Area of Ghana. Proceed. Int. Acad. Ecol. Environ. Sci. 2 (3), 177–192.
O'conor, J. T., 1965. A classification for quartz-rich igneous rock based on feldspar ratios. U.S. Geological Survey Professional Paper 525B, B79–B84.
Parra-Avila, L.A., Kemp, A.I.S., Fiorentini, M.L., Belousova, E., Baratoux, L., Block, S., Jessell, M., Bruguier, O., Begg, G.C., Miller, J., Davis, J., McCuaig, T.C., 2017. The geochronological evolution of the Paleoproterozoic Baoulé-Mossi domain of the Southern West African Craton. Precambrian Res. 300, 1–27.
Parra-Avila, L.A., Belousova, E., Fiorentini, M.L., Eglinger, A., Block, S., Miller, J., 2018. Zircon Hf and O-isotope constraints on the evolution of the Paleoproterozoic Baoulé-Mossi domain of the southern West African Craton. Precambrian Res. 306, 174–188.
Patino Douce, A.E., 1993. Titanium substitution in biotite: an empirical model with applications to thermometry, O_2 and H_2O barometries and consequences form biotite stability. Chem. Geol. 108, 133–162.
Pearce, J.A., Harris, N.B.W., Tindle, A.G., 1984. Trace element discrimination diagrams for the interpretation of granitic rocks. J. Petrol. 25, 956–983.
Peccerillo, A., Taylor, S.R., 1976. Geochemistry of eocene calc-alkaline volcanic rocks from the Kastamonu Area, Northern Turkey. Contrib. Mineral. Petrol. 58, 63–81.
Petersson, A., Scherstén, A., Gerdes, A., 2018. Extensive reworking of Archaean crust within the Birimian terrane in Ghana as revealed by combined zircon U-Pb and Lu-Hf isotopes. Geosci. Front. 9, 173–189.
Petersson, A., Scherstén, A., Kemp, A.I.S., Kristinsdottir, B., Kalvig, P., Anum, S., 2016. Zircon U-Pb-Hf evidence for subduction related crustal growth and reworking of Archaean crust within the Paleoproterozoic Birimian terrane, West African Craton, SE Ghana. Precambrian Res. 275, 286–309.
Pohl, D., Carlson, C., 1993. A plate tectonic re-interpretation of the 2.2–2.0 Ga Birimian province, Tarkwaian System and metallogenesis in West Africa. In: Peters, J.W., Kesse, G.O., Acquah (Eds.), Regional trends in African geology. Geological Society of Africa, Accra, pp. 378–381.
Rogers, J.J.W., Santosh, M., 2002. Configuration of Columbia, a mesoproterozoic supercontinent. Gondwana Res. 5, 5–22.
Rogers, J.J.W., Santosh, M., 2009. Tectonics and surface effects of the supercontinent Columbia. Gondwana Res. 15, 373–380.
Sakyi, P.A., Anum, S., Su, B.-X., Nude, P.M., Su, B.-C., Asiedu, D.K., Nyame, F., Kwayisi, D., 2017. Geochemical and Sr-Nd isotopic records of Paleoproterozoic metavolcanics and mafic intrusive rocks from the West African Craton: evidence for petrogenesis and tectonic setting. Geol. J. 52, 725–741.
Sakyi, P.A., Su, B.-N., Anum, S., Kwayisi, D., Dampare, S.B., Anani, C.Y., Nude, P.M., 2014. New zircon U-Pb ages for erratic emplacement 2203–2130 Ma Paleoproterozoic calc-alkaline I-type granitoid rocks in the Lawra volcanic belt of Northwestern Ghana, West Africa. Precambrian Res. 254, 149–168.
Schmidt, M.W., 1992. Amphibole composition in tonalite as a function of pressure: an experimental calibration of the Al-in hornblende barometer. Contrib. Mineral. Petrol. 110, 304–310.
Su, B.X., Zhang, H.F., Deloule, E., Vigier, N., Hu, Y., Tang, Y.J., Xiao, Y., Sakyi, P.A., 2014. Distinguishing silicate and carbonatite mantle metasomatism by using lithium and its isotopes. Chem. Geol. 381, 67–77.
Sylvester, P.J., 1994. Archean granite plutons. In: Condie, K.C. (Ed.), The Archean Crustal Evolution. Elsevier, Amsterdam, pp. 261–314.
Sylvester, P.J., Attoh, K., 1992. Lithostratigraphy and composition of 2.1 Ga greenstone belts of the West African craton and their bearing on crustal evolution and Archean-Proterozoic boundary. J. Geol. 100, 377–393.
Taylor, N.P., Moorbath, S., Leube, A., Hirdes, W., 1992. Early Proterozoic crustal evolution in the Birimian of Ghana: constraints from geochronology and isotope geochemistry. Precambrian Res. 56, 97–111.
Taylor, S.R., McLennan, S.M., 1985. The continental crust: Its composition and evolution. Blackwell Scientific Publications, Oxford, pp. 312.
Vidal, M., Gumiaux, C., Cagnard, F., Pouclet, A., Ouattara, G., Pichon, M., 2009. Evolution of a Paleoproterozoic "weak type" orogeny in the West African Craton (Ivory Coast). Tectonophysics 477, 145–159.
Wane, O., Liégeois, J.P., Thébaud, N., Miller, J., Metelka, V., Jessell, M., 2018. The onset of the Eburnean collision with the Kenema-Man craton evidenced by plutonic and volcano-sedimentary rock record of the Masssigui region, southern Mali. Precambrian Res. 305, 444–478.
Watkins, J.M., Clemens, J.D., Treloar, P.J., 2007. Archaean TTGs as sources of younger granitic magmas: melting of sodic metatonalites at ca. 0.6-1.2 GPa. Contrib. Mineral. Petrol. 154, 91–110.
Whalen, J.B., Currie, K.L., Chappell, B.W., 1987. A-type granites: geochemical characteristics, discrimination and petrogenesis. Contrib. Mineral. Petrol. 95, 407–419.
Winter, J.D., 2001. An Introduction to Igneous and Metamorphic Petrology. Prentice Hall 1–699.
Wolf, M.B., Wyllie, J.P., 1994. Dehydration-melting of amphibolite at 10 Kbar: the effects of temperature and time. Contrib. Mineral. Petrol. 115, 369–383.
Wright, J.B., Hastings, D.A., Jones, W.B., Williams, H.R., 1985. Geology and Mineral Resources of West Africa. George Allen and Unwin, Boston, pp. 187.
Zhang, H.F., Sun, M., Zhou, X.H., Fan, W.M., Zhai, M.G., Yin, J.F., 2002. Mesozoic lithosphere destruction beneath the North China Craton: evidence from major, trace element, and Sr-Nd-Pb isotope studies of Fangcheng basalts. Contrib. Mineral. Petrol. 144, 241–253.
Zhao, G., Cawood, P.A., Wilde, S.A., Sun, M., 2002. Review of global 2.1–1.8 Ga collisional orogens and accreted cratons: a pre-Rodinia supercontinent? Earth Sci. Rev. 59, 125–162.
Zhao, G., Sun, M., Wilde, S.A., Li, S., 2004. A Paleo-Mesoproterozoic supercontinent: Assembly, growth, and breakup. Earth Sci. Rev. 67, 91–123.
Zhao, J.-H., Zhou, M.-F., 2007. Geochemistry of Neoproterozoic mafic intrusions in the Panzhihua district (Shichuan Province, SW China): Implications for subduction-related metasomatism in the upper mantle. Precambrian Res. 152, 27–47.
Zindler, A., Hart, S., 1986. Chemical geodynamics. Ann. Rev. Earth Planet. Sci. 14, 493–571.